4

UCRL- 94997
PREPRINT

PHYSICS OF DENSE FLUIDS

Marvin Ross
Lawrence Livermore National Laboratory
University of California
Livermore, CA 94550

CIRCULATION COPY
SUBJECT TO RECALL
IN TWO WEEKS

This paper was prepared for the
NATO Advanced Study Institute
"Advances in High Pressure Studies on Chemical and Biochemical Systems"
Corfu, Greece

July 1986

Lawrence
Livermore
National
Laboratory

This is a preprint of a paper intended for publication in a journal or proceedings. Since changes may be made before publication, this preprint is made available with the understanding that it will not be cited or reproduced without the permission of the author.

DISCLAIMER

This document was prepared as an account of work sponsored by an agency of the United States Government. Neither the United States Government nor the University of California nor any of their employees, makes any warranty, express or implied, or assumes any legal liability or responsibility for the accuracy, completeness, or usefulness of any information, apparatus, product, or process disclosed, or represents that its use would not infringe privately owned rights. Reference herein to any specific commercial products, process, or service by trade name, trademark, manufacturer, or otherwise, does not necessarily constitute or imply its endorsement, recommendation, or favoring by the United States Government or the University of California. The views and opinions of authors expressed herein do not necessarily state or reflect those of the United States Government or the University of California, and shall not be used for advertising or product endorsement purposes.

PHYSICS OF DENSE FLUIDS

Marvin Ross
Lawrence Livermore National Laboratory
Physics Department, H-Division
P.O. Box 808
Livermore, Ca 94550, USA

ABSTRACT.

We review recent advances in the theory of dense fluids and of the application of these methods to the study of shock compressed liquids.

I. INTRODUCTION

In the present article we examine the properties of liquids and fluids at high pressure and temperature with special emphasis on theoretical and shockwave studies. The extremely high pressures and temperatures generated in shockwave experiments on liquids provides the theorist with a unique opportunity to study intermolecular forces, electronic and chemical properties, and melting at extreme conditions.

In a shockwave experiment one measures the shock and particle velocities and from these the pressure and density of the final state can be obtained directly. For some materials it is also possible to measure temperature and optical properties. But for the most part detailed information about atomic and molecular processes must come from theoretical studies. It is the responsibility of the theoretician to interpret the experimental results in terms of microscopic physics and to extract additional information and insight.

This article is organized into three main sections. Section 2 is a review of some of the theoretical and computational methods that are useful in the study of dense fluids. In section 3 we introduce the fundamental relations of shock physics. Section 4 will be devoted to examining the application of liquid theory to the interpretation of shock data.

2. THEORY OF FLUIDS AT HIGH PRESSURE

The most important advances in the theory of fluids have come from computer simulations and the development of computationally fast approximate models. For a number of well-defined potentials, simulations carried out by Monte Carlo and molecular dynamics methods have been used to determine the pair distribution and thermodynamic and transport properties over a wide range of conditions. An extensive set of data exists for the hard sphere, Lennard-Jones and inverse-power potentials.

Computer simulations should be viewed as experiments producing exact data which complement laboratory experiments. For the case of strongly coupled degenerate plasmas with densities comparable to those found in high-energy astrophysics and laser-fusion-compression experiments, computer simulations are the only 'experimental' data. Computer simulation results have been extremely valuable in the development and testing of approximate methods such as variational fluid theory and the hypernetted chain method. These methods are now 'work horses' for applications to simple fluids and dense plasmas. For a detailed review of liquid theory, computer methods and results, see Barker and Henderson[1] and Hansen and McDonald.[2] Although computer simulations provide a sound basis for statistical theories, they typically deal with idealized systems. The physically interesting atomic and electronic processes must be introduced separately with approximate models.

But in addition to accurate statistical mechanical theories the determination of real fluid properties requires a detailed description of the intermolecular forces. From a rigorous point of view this part of the problem is in the least satisfactory state. Almost all useful intermolecular potentials are at least semiempirical having been obtained in some way from experimental information.

In this section we first discuss the computer simulations which provide "exact" results but which are slow and expensive and then examine several approximate methods which are, computationally fast and have been tested for accuracy against the computer simulations. We close this section with some remarks regarding intermolecular potentials.

2.1 Computer Simulations

The two principal computer simulation methods are Monte Carlo and molecular dynamics. In the Monte Carlo method, random sampling techniques are used in which particles are moved and an ensemble of possible configurations is generated. Thermodynamic properties are obtained by averaging the properties of these configurations. In molecular dynamics the ensemble of configurations is obtained by directly integrating the complete set of Newton's equations of motion. Despite these fundamental differences the methods have several common features. In both, N molecules are confined to a box of volume V at temperature T. Computer size and speed limits N to several hundred particles. To minimize surface effects periodic boundary conditions are employed. This consists of filling three dimensional space by replications of the original cell in which the molecules in each cell occupy the same relative positions.

The initial or starting configuration may be ordered or random. The potential energy or force exerted on a particle is computed by

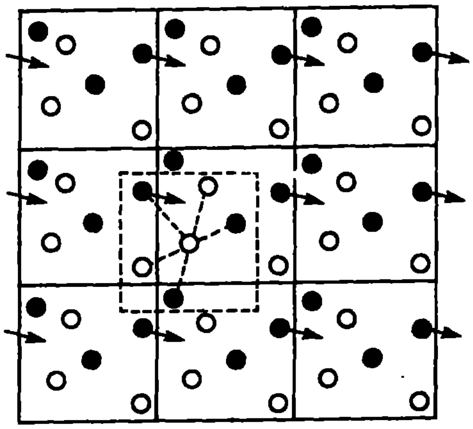

Fig 2.1. A two dimensional periodic system. Each particle in the central box interacts with its nearest neighbors in the same or in a neighboring cell as defined by the dashed lines. If a particle moves outside the central cell, then its counterpart in an adjacent cell moves in through the opposite boundary. One can assess the validity of the periodic boundary conditions by repeating the simulations using different numbers of particles.

summing over the interactions with nearest neighbors in the same and adjoining cells.

In the Monte Carlo method a particle, chosen at random, is moved from position (x,y,z) to (x, + δx, y + δy, z + δz) by randomly choosing δx, δy, and δz. The change in potential energy δU is computed and if the move results in a decrease in energy the new configuration is accepted and its properties are included in the ensemble averaging. If the energy increases the computer selects a random number between 0 and 1 and compares it with exp $(-\delta U/kT)$. The move is allowed if the random number is the smaller, otherwise the move is rejected and the previous configuration counted again. The properties of the system are obtained by taking the ensemble average over all configurations.

In the molecular dynamics technique the velocities and positions for all N interacting particles are determined by solving Newtons equations. The molecular dynamics technique has the advantage that it can be used for studying non-equilibrium processes provided the characteristic relaxation times are significantly shorter than the computer time ($\sim 10^{-11}$ seconds). The equilibrium properties determined by Monte Carlo and molecular dynamics are in excellent agreement. The free energy and entropy can be determined for a state of interest by a thermodynamic integration along a path connecting to one in which the free energy is known. For example by integrating from the gas along a reversible path to the liquid.

Constant pressure molecular dynamics and Monte Carlo simulations as opposed to the constant volume methods described above, have been increasingly used to study high pressure solid-solid phase transitions.[3] The new method allows the system to change both its volume and shape in response to an imbalance in the forces and permits the detailed study of the mechanics of a transition.

Some Monte Carlo Results

The first molecular dynamics calculations were made for hard-sphere systems. This potential is

$$\phi(r) = \infty, \ r \leq d,$$

and

$$\phi(r) = 0, \ r > d. \tag{2.1}$$

where d is the hard sphere diameter. Thus the dynamics breaks down into a series of "billiard ball" collisions following which molecules move in straight lines. The pressure data in the fluid (Fig. 2.2) may be expressed as

$$\frac{\beta P}{\rho} = (1 + \eta + \eta^2 - \eta^3)/\ (1 - \eta)^3 \quad , \tag{2.2}$$

where $\eta = (\pi/6)\rho d^3$, $\beta = 1/k_BT$, k_B is the Boltzmann's constant and ρ is the number of particles per unit volume. η is the hard sphere packing fraction. The excess Helmholtz free energy per molecule, A, can be obtained from

$$\frac{\beta A}{N} = \int_0^{\rho} \{\frac{\beta P}{\rho'} - 1\} \frac{d\rho'}{\rho'} + \log \rho - 1 \tag{2.3}$$

which leads to

$$\frac{A_{HS}}{NkT} = \frac{4\eta - 3\eta^2}{(1 - \eta)^2} \tag{2.4}$$

This expression is referred to as the Carnahan-Starling[4] hard sphere

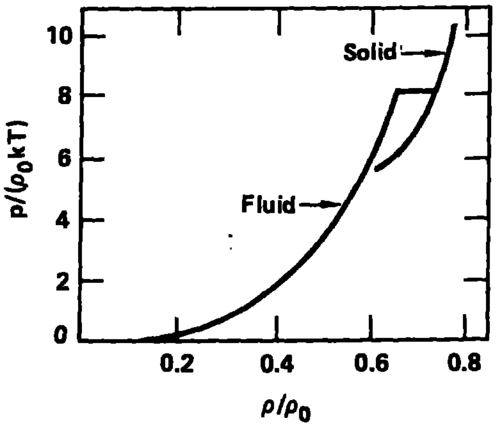

Fig. 2.2. Equation of state of hard sphere system. The quantity ρ_0 is the close-packed density.

free energy. Although the hard sphere system is an idealized model it is a very useful prototype and widely used as a reference system for fluids. More realistic systems have softer repulsions. Extensive computer results also exist for systems fo particles interacting through the softer inverse power potential, $\phi(r) = \epsilon(r^*/r)^n$ for n = 12, 9, 6, 4 and 1 and the more realistic Lennard-Jones (LJ) potential, $\phi(r) = \epsilon[r^*/r)^{12} - 2(r^*/r)^6]$. Simple analytic expressions have been fitted to these "experimental" data which permit rapid evaluation of thermodynamic properties.[5]

2.2 Fluid Variational Theory

A number of approximate methods have been developed for calculating liquid properties. They have invariably been derived from a perturbation theory in which the properties of the reference system is well known. The most widely used reference system is the hard sphere fluid. At high pressures many of these standard perturbation theories have serious short comings. In this section we limit ourselves to those which have proven useful at high pressures as validated by testing against computer simulations and successful applications to the study of dense liquids. The most useful treatment of high pressure liquids has been with variational theory.

In the variational formulation of perturbation theory the Helmholtz free energy A of an interacting system is approximated by the use of the Gibbs-Bogolyubov inequality:

$$A \leq A_0 + \langle \phi - \phi_0 \rangle_0 \quad . \tag{2.5}$$

This equation states that the free energy of the interacting system is bounded above by the free energy of a reference system (A_0) plus the difference in potential energy between the actual system and the reference, averaged over all configurations of the reference system.

The reference system of virtually unanimous choice has been the hard sphere. This system represents the limiting case of particles interacting by a repulsive potential and has been well characterized by the systematic molecular dynamic computer studies. Analytic expressions for $A_{HS}(d,\rho)$ and the pair distribution function $g_{HS}(r/d,\rho)$ have been obtained, as a function of ρ and d from computer data. Closed-form analytic approximations to g_{HS} have also been derived from solutions of the Percus-Yevick equations. For more details see reference 1. Consequently, the problem becomes to a large measure how to choose the hard-sphere diameter. It is chiefly the manner in which this choice is made that distinguishes the various perturbation theories.

Mansoori and Canfield were the first to use hard spheres as a reference system in a variational theory. The excess Helmholtz free energy of the fluid reduces to

$$A \leq A_{HS} + \frac{N}{2} \rho \int_0^\infty g_{HS}(r, \eta)\, \phi(r) d^3r \quad , \tag{2.6}$$

where A_{HS} and g_{HS} are the free energy and pair distribution function of the reference system. Whereas hard spheres have many attractive features, they incorporate a repulsion that tends to be unrealistically severe at high density and hence limits their accuracy.

Soft Sphere Variational Theory[6]

A more realistic system is the inverse 12th-power or soft sphere (SS) reference potential. For this system, the excess Helmholtz free energy may be written as the inequality

$$A \le A_{12}(\lambda) + \frac{N}{2} \rho \int_0^\infty g_{12}(r, \lambda)\, [\phi(r) - \phi_{12}(r)]\, d^3r \tag{2.7}$$

where λ is some characteristic parameter of the reference system which minimizes the right side of Eq. 2.7. Judging from the usefulness of the hard-sphere packing fraction η as a universal fluid scaling parameter, it is tempting to relate the parameter λ to η and express the reference-state properties as functions of η. We may approximate A_{12} in terms of hard sphere theory by using the equation

$$A_{12} \le A_{HS} + \frac{N}{2} \rho \int_d^\infty g_{PY}(r, \eta)\, \phi_{12}(r)\, d^3r \quad . \tag{2.8}$$

where g_{PY} is the Percus-Yevick approximation to the hard sphere pair distribution function.

Listed in Table 2.1 are Helmholtz free energies for the inverse 12th-power system as determined from the Monte Carlo calculations of Hoover et al.[7] and Hansen.[8] These are shown in columns 2 and 3,

TABLE 2.1. Comparison of inverse 12th-power excess Helmholtz free energies from Monte Carlo calculations (MC), fitted with soft sphere theory using Eq. (2.8), and from hard sphere theory using Eq. 2.9.

$\rho(\varepsilon/kT)^{1/4}$	MC[a]	MC[b]	Eq. (2.9)	Eq. (2.8)
0.1	0.40	0.40	0.40	0.44
0.2	0.91	0.91	0.90	0.99
0.3	1.53	1.53	1.52	1.67
0.4	2.32	2.33	2.32	2.53
0.5	3.33	3.34	3.32	3.60
0.6	4.60	4.61	4.60	4.93
0.7	6.20	6.21	6.20	6.60
0.8	8.19	8.21	8.20	8.67

[a] Results from Hoover et al., Ref. 7.
[b] Results from Hansen, Ref. 8.

respectively. In column 5 are results computed by the hard sphere variational method using Eq. (2.8). The agreement is of the order of 8%. We now determine a function of η which, when added to the RHS of Eq. (2.8) and included in the variational procedure, will result in computed properties that agree exactly with the Monte Carlo results. $F_{12}(\eta) = -(\eta^4/2 + \eta^2 + \eta/2)$ is such a function. The free energy calculated with Eq. 2.9 is shown in column 4 of Table 2.1. Thus the free-energy function which reproduces the Monte Carlo inverse 12th-power results exactly in terms of hard-sphere parameters, is

$$A_{12} \leq A_{HS} + \frac{N}{2} \rho \int_d^\infty g_{PY}(r, \eta)\, \phi_{12}(r)\, d^3r + F_{12}(\eta)\, NkT \quad . \tag{2.9}$$

We now replace $A_{12}(\lambda)$ in Eq. (2.7) by $A_{12}(\eta)$, and the full expression for A becomes

$$A \leq A_{HS} + \frac{N}{2} \rho \int_d^\infty g_{PY}(r, \eta)\, \phi_{12}(r)\, d^3r$$

$$+ F_{12}(\eta)\, NkT + \frac{N}{2} \rho \int_0^\infty g_{12}(r, \lambda)\, [\phi(r) - \phi_{12}(r)]\, d^3r \tag{2.10}$$

It contains terms with $g_{12}(r, \lambda)$ and $g_{PY}(r, \eta)$. We approximate g_{12} with g_{PY} and by combining the second and fourth terms, Eq. (2.10) is rewritten as

$$A \leq A_{HS} + \frac{\rho N}{2} \int_d^\infty g_{PY}(r, \eta)\, \phi(r)\, d^3r + F_{12}(\eta)\, NkT, \tag{2.11}$$

This equation is formally identical to the original hard-sphere variational formulation except for the additional term, $F_{12}(\eta)$. This term modifies the hard sphere system in such a manner as to convert it to an inverse twelfth power reference preserving the usefulness of η and the analyticity of g_{HS}. The η is chosen to have the value that minimizes the Helmholtz free energy. The pressure (P) and excess internal energy (U) are obtained by taking the derivatives of A:

$$\beta P/\rho = 1 + \rho \left(\frac{\partial \beta A}{\partial \rho}\right)_T \quad , \tag{2.12}$$

$$\beta U = \beta \left(\frac{\partial \beta A}{\partial \beta}\right)_\rho \quad . \tag{2.13}$$

Young and Rogers[9] have constructed a thermodynamically consistent inverse 12th power fluid variational theory (I12) which uses an accurate fit to the reference fluid free energy and tabulated accurate reference fluid radial distribution functions computed from a new integral equation. In reduced variables, where $x = r/a$, $a = (3/4\pi\rho)^{1/3}$

Table 2.2. Comparison of theoretical (I12 and SS) and simulation (EX) reduced total pressures and reduced excess internal energies for the Lennard-Jones fluid.[9] $T^* = kT/\varepsilon$ and $\rho^* = \rho\, r^{*3}/\sqrt{2}$.

			PV/NkT			U/NkT	
T*	ρ*	EX	I12	SS	EX	I12	SS
100	0.2	1.221	1.225	1.216	0.036	0.037	0.034
	0.5	1.675	1.682	1.669	0.115	0.117	0.111
	1.00	2.95	2.98	2.96	0.361	0.366	0.358
	2.0	9.50	9.51	9.57	1.767	1.772	1.779
	2.5	16.29	16.45	16.55	3.304	3.350	3.365
20	0.2	1.270	1.272	1.258	-0.005	-0.002	-0.010
	0.5	1.930	1.947	1.922	0.026	0.034	0.018
	1.333	7.999	8.031	8.089	0.942	0.960	0.958
	1.765	16.68	16.66	16.75	2.65	2.65	2.66
5	0.2	1.169	1.177	1.149	-0.202	-0.178	-0.200
	0.5	1.867	1.859	1.822	-0.474	-0.448	-0.488
	1.00	6.336	6.437	6.491	-0.456	-0.422	-0.448
	1.279	13.44	13.37	13.46	0.435	0.430	0.413
2.74	0.1	0.97	1.00	0.97	-0.223	-0.174	-0.199
	0.3	1.04	1.07	1.01	-0.650	-0.580	-0.630
	0.55	1.65	1.62	1.60	-1.172	-1.122	-1.181
	1.00	7.37	7.27	7.37	-1.525	-1.525	-1.559
	1.10	10.17	10.23	10.30	-1.351	-1.313	-1.352
1.35	0.1	0.72	0.76	0.75	-0.578	-0.383	-0.423
	0.3	0.35	0.35	0.27	-1.548	-1.284	-1.374
	0.5	0.30	0.18	0.14	-2.496	-2.327	-2.430
	0.9	4.58	4.52	4.60	-4.192	-4.144	-4.220
	0.95	6.32	6.00	6.08	-4.230	-4.239	-4.311
0.810	0.801	0.057	-0.058	0.073	-7.068	-6.963	-7.074
	0.8839	1.946	2.106	2.122	-7.707	-7.580	-7.687
0.72	0.8350	-0.080	-0.182	0.019	-8.400	-8.285	-8.391
	0.9158	2.248	2.614	2.687	-9.079	-8.909	-9.031

and $z = (Nr^{*3}/\sqrt{2}\ V)(\varepsilon/kT)^{1/4}$, the variational inequality becomes

$$\frac{A}{NkT} \leq \frac{A_{12}(z)}{NkT} + \frac{3}{2}\int_0^\infty \left[\frac{\phi(r)}{kT} - \frac{\Gamma}{x^{12}}\right] g_{12}(x,\ z)\, x^2\, dx, \qquad (2.14)$$

where $\Gamma = 4\ \sqrt{2}\pi z/3)$ is the variational parameter used to minimize the right-hand side of Eq. (2.14). Values of $g_{12}(x,\ z)$ for arbitrary z are determined by using cubic spline interpolation in z space. Pressure and energy are then determined by numerical differentiation of the free energy with respect to volume and temperature, respectively.

RESULTS OF CALCULATIONS

Calculations for the thermodynamic properties of the fluid theories were carried out and the results were compared with computer experiments for two potentials--the Lennard-Jones (LJ)

$$\phi(r) = \varepsilon\left[\left(\frac{r^*}{r}\right)^{12} -2\left(\frac{r^*}{r}\right)^{6}\right] , \qquad (2.15)$$

and the exponential-six (exp-6)

$$\phi(r) = \varepsilon\left[\left(\frac{6}{\alpha - 6}\right) \exp[\alpha(1 - r/r^*)] - \left(\frac{\alpha}{\alpha - 6}\right)\left(\frac{r^*}{r}\right)^{6}\right] . \qquad (2.16)$$

The results for the Lennard-Jones potential are shown in Table 2.2 and are compared with the Monte Carlo simulations here. Similar agreement was found using the exponential-six using $\alpha = 13.5$.[9]

The results show that the soft sphere and inverse-12th variational theories are in good overall agreement with computer simulations of various model fluids. The agreement between theory and simulation is excellent at high pressure near the melting curve. SS theory, which is really an approximation to the I12 theory, useful as a practical method for calculating fluid properties. An advantage of the SS theory is the use of an analytic $g_{HS}(r, \eta)$ subroutine, which avoids the problem of interpolation errors with tabular functions. For most applications the marginal improvement of I12 theory may not justify the additional computational complexity.

Although perturbation theories are fast and convenient and give good results for thermodynamic properties they do not predict accurate structural properties. The integral equations such as the modified hypernetted chain (HNC) equation are more complicated computationally but as a result of several recent advances they can now be made to yield thermodynamic and structural properties in excellent agreement with computer simulations. Integral equations are also more directly applicable to mixtures and to ionic systems than are perturbation theories. A complete discussion the integral equations are beyond the scope of this review, but a good comparison of this method and variational has been reported by Talbot et al.[10]

2.3 Intermolecular Potentials at High Density.

Among the least satisfactory features of liquid physics has been the difficulty in obtaining accurate intermolecular forces from first principles. Typically the forces calculated between pairs of molecules are too stiff when used at high densities because they neglect many-body interactions. The case of H_2 illustrates this well. Figure 2.3 compares the H_2-H_2 pair potential determined from quantum-mechanical calculations with that derived from shock data.

For many dense liquids a useful semiempirical potential is the exp-six (Eq. 2.16), where α, r^* and ε are adjustable parameters, typically obtained by fitting to experimental data, which determine

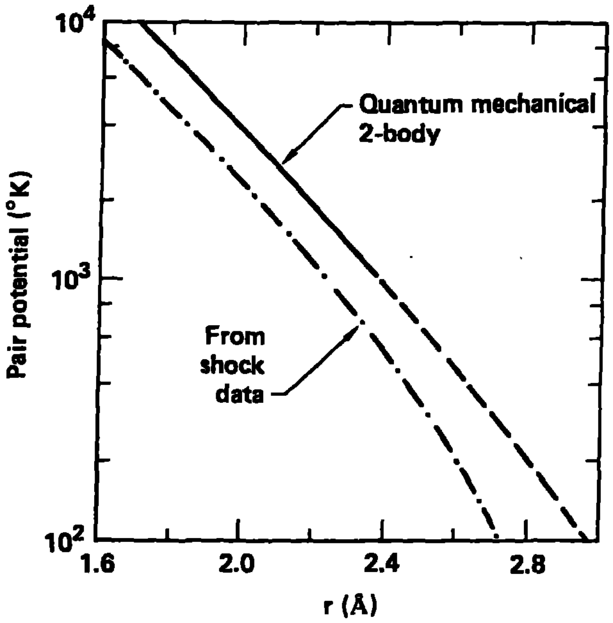

Fig. 2.3. Many-body effects in H_2-H_2 potential. Comparison of the hydrogen pair potential obtained from ab initio H_2-H_2 calculations with one obtained from shock data.

the repulsive stiffness, the position of the potential minimum and its depth. The exponential term is a more realistic characterization of interatomic repulsive forces than the inverse twelfth power (Lennard-Jones) potential. At very small separations the attraction may become unrealistically large. This can be avoided by multiplying the attractive term by a damping function.

A good example of such a procedure is to be found in the widely used Aziz potential for helium.[11] The form of the potential is

$$V(r) = \varepsilon V^*(x)$$

$$V^*(x) = A \exp(-\alpha x) - \left(\frac{C_6}{x^6} + \frac{C_8}{x^8} + \frac{C_{10}}{x^{10}} \right) F(x) \quad , \qquad (2.17)$$

where

$$F(x) = \exp\left[- \left(\frac{D}{x} - 1 \right)^2 \right] \text{for } x < D$$

$$= 1 \qquad\qquad \text{for } x \geq D$$

and $D = 1.28$ and $x = r/r_m$.

The function F(x), which is considered to be universal for all spherical systems, was obtained by fitting a potential of this form to the accurately known potential curve of the $^3\Sigma_u^+$ state of H_2. This fixed the value of parameter D.

The input data for this potential are the SCF HF calculations of the repulsive interaction, C_6, C_8 and C_{10} are the multipole dispersion coefficients. The parameters $\epsilon/k = 10.8$ K and $r_m = 2.98$ Å result from constraints on the value of the reduced potential and its slope at its minimum. The value of α may be determined from scattering data or fitted to Hartree Fock results at small r.

A considerable simplification in the choice of potential parameters for shock-compressed molecular fluids has emerged from the recognition that the repulsive pair potentials approximately obey the corresponding-states scaling principle.[12] That is, for two fluids the ratios of the depths of their potential wells (ϵ) are in the same ratio as their critical temperatures (T), and the cubes of their characteristic length scales (r^*) are in proportion to their critical volumes (V_c). As a result of having fitted parameters to the Ar potential, it has been possible to predict within experimental error the Hugoniot curves for most molecular liquids. This means that the repulsive forces which dominate the high-temperature properties have similar functional dependencies for most fluids. An exception is hydrogen, which has a much softer repulsive force than other closed-shell molecules.

3. SHOCK COMPRESSION

A shock wave is a disturbance propagating at supersonic speed in a material, preceded by an extremely rapid rise in pressure, density and temperature. The general reader often associates shock waves with explosions and other uncontrolled and irreversible processes. Although shock waves are irreversible, the process is well understood and can be controlled to produce a desired response. Shock compression studies obtain high pressures by introducing a rapid impulse through the detonation of a high explosive, the impact of a high-speed projectile or the absorption of an intense pulse of radiation. A shock wave not sustained loses energy through viscous dissipation and reduces to a sound wave (e.g., thunder). High-speed optical and electronic methods are necessary to measure certain dynamic variables which determine pressure, density and energy. In shock-wave experiments, the passage time of the shock is short compared ot the disassembly or 'fly away' time of the sample. As a result the attainable pressures for a given material are limited only by the energy density supplied by the driver. Chemical explosives have been used to obtain pressures up to 1 Mbar in liquids and up to 13 Mbar in metals, with accompanying temperatures of tens of thousands of degrees Kelvin. Final pressures ranging from 20-158 Mbar have been reported using underground nuclear explosions. In inertial confinement studies, pellets of liquid deuterium are subjected briefly to laser-driven dynamic pressures of about 1000 Mbar and temperatures in excess of 10^7 K. An excellent introduction to shock wave physics is to be found in Zeldovich and Raizer.[13]

3.1 Introduction to the Dynamics of Shockwaves

Consider a fluid or solid at rest with constant density and pressure, ρ_0, Po bounded on the left by a plane piston in a cylinder of area A.

Let us assume that at t_0 the piston is set in motion with a constant velocity u_p. This motion compresses the material before it and a disturbance with velocity propagates in the direction. The first infinitesimal compression at the piston face results in the propagation of a sound wave with velocity C. However, subsequent compressions at the piston face take place with the material at higher densities and result in higher local sound speeds. This produces a train of waves in which the first is at the speed of sound in the undisturbed material and the last, closest to the piston face, is supersonic. Because the last wave can catch but not pass the first, all the waves eventually coalesce into a single, steep steady wave front across which exists a sharp discontinuity in pressure, density, and temperature. The width of the discontinuity is generally a few molecular mean-free-path lengths.

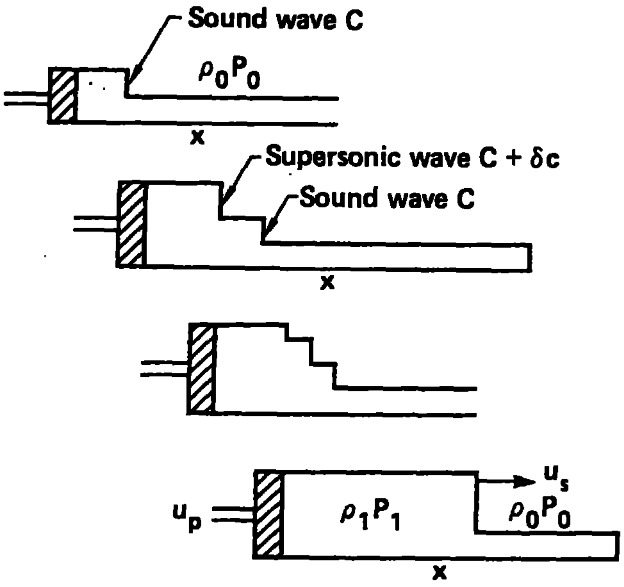

Fig. 3.1. Formation of a one-dimensional planar shock wave. Shown by pressure-density-distance p-x plots at successive times.

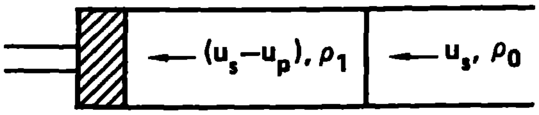

Fig. 3.2. Steady shock wave as viewed by an observer on the shock front. The fluid streams toward the shock front at a velocity u_s and rushes to the left away at the velocity u_s-u_p.

We can now apply the general laws of conservation of mass, momentum and energy to determine the pressure, density and velocity of the disturbance.

A useful coordinate system is shown in Fig. 3.2 in which the observer is moving with the shockfront.

During a period δt a mass of $\rho_0 u_s A\delta t$ passes through the shockfront. Conservation of mass requires that

$$\rho_0 u_s A\delta t = \rho_1(u_s - u_p)\, A\delta t$$

$$\rho_0 u_s = \rho_1(u_s - u_p) \tag{3.1}$$

This leads to an expression for the density change

$$\frac{\rho_0}{\rho_1} = 1 - \frac{u_p}{u_s} \quad . \tag{3.2}$$

The pressure jump across the shock may be determined from the conservation of momentum. To the observer the momentum flow from the unshocked fluid into the shockfront is

$$(\rho_0 u_s\, A\delta t)\, u_s \quad .$$

The momentum flow away from the shockfront is

$$\rho_1(u_s - u_p)\, A\delta t\, (u_s - u_p) \quad ,$$

or using Eq. 3.1

$$\rho_0 u_s\, A\delta t\, (u_s - u_p) \quad .$$

The change in momentum must equal the difference in forces across the front $(P_1 - P_0)\, A\delta t$. Thus conservation of momentum leads to an expression for the pressure change.

$$P_1 - P_o = \rho_o u_s u_p \quad . \tag{3.3}$$

Similarly the law of conservation of energy.

$$\rho_1(u_s - u_p)\left[E_1 + \frac{P_1}{\rho_1} + \frac{(u_s - u_p)^2}{2}\right] = \rho_o u_s \left[E_o + \frac{P_o}{\rho_o} + \frac{u_s^2}{2}\right] .$$

leads to the energy equation.

$$E_1 - E_o = \frac{1}{2}\,(P_1 + P_o)\,(V_o - V) \quad , \tag{3.4}$$

in which we introduced the specific volumes $V_0 = 1/\rho_0$ and $V_1 = 1/\rho_1$ in place of density. Equations 3.2-3.4 are referred to as the Hugoniot equations.

The derivation of these equations considers the shockfront as a

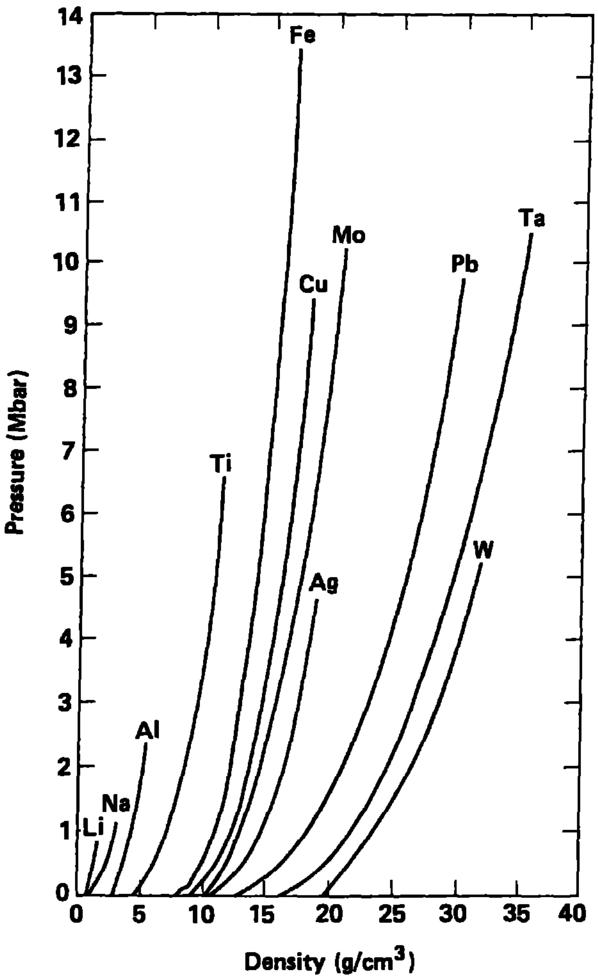

Fig. 3.3. Experimental Hugoniots for metals.

discontinuity but says nothing of its width. Only the equilibrium properties on either side are considered in the flow properties.

The Hugoniot equations represent the locus of all final states that can be reached by shock-compressing a material from a given initial state; the resultant curve of pressure against volume is known as a Hugoniot. If the initial state is known, then the final-state properties may be determined from a measurement of any two of these five properties (u_s, u_p, P, ρ, E). Of these, the shock and particle velocities are the most commonly measured. A discussion of experimental methods is beyond the scope of the present review. For the interested reader a complete description of the shock wave techniques for liquids has been given by Nellis and Mitchell.[14]

Shock-wave measurements have been carried out on most elements on a very large number of compounds. The most extensive single source of all published Hugoniot data up to 1977 is the LLNL Compendium of Shock Wave Data by van Thiel et al.[15] Marsh has made available all of the

Los Alamos data including previously unreported measurements.[16] These two collections include data for elements, alloys, rocks, minerals and compounds, plastics and synthetics, woods, assorted liquids, aqueous solutions and high explosives. Al'tshuler et al. have reported a critical analysis of shock measurements for most of the metals.[17]

The assumptions made in deriving the Hugoniot equations were one-dimensional steady motion, thermodynamic equilibrium immediately ahead of an behind the shock front, and negligible material strength. The first assumption can be met experimentally. The second will hold if the relaxation times are much less than the resolution of the detectors ~ 10 ns. The third is justified for pressures appreciably greater than the yield strength of the material. Typical yield strengths in metals are 20 kbar and much less for most materials. In the case of liquids, which have no yield strength, this creates no problem. The temperature cannot be obtained from the Hugoniot equations, but must be derived from an equation of state. In a few cases it has been determined from a direct measurement of the emitted radiation.

Several equations of general interest follow from the conservation laws. In place of energy we introduce the enthalpy H = E + PV. We can write the Hugoniot equation in the equivalent form

$$H_1 - H_o = \frac{1}{2} (P_1 - P_o) (V_o + V_1) \quad . \tag{3.5}$$

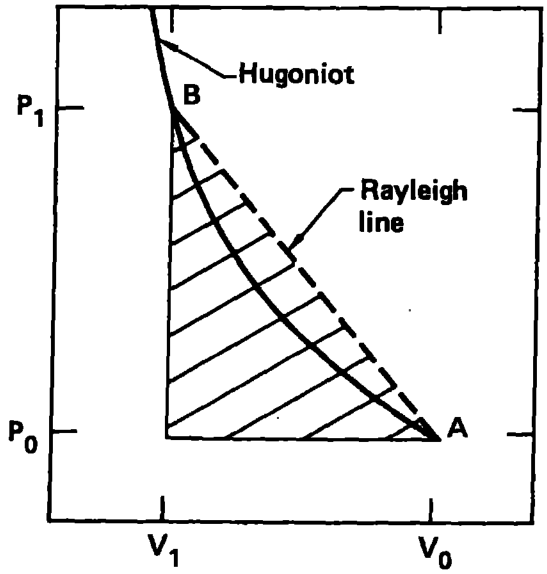

Fig. 3.4. The crosshatched area represents the piston kinetic energy and is the total energy transmitted by the piston to a unit mass initially at rest.

Eqs: 3.2 and 3.3 can be combined to obtain explicit expressions for the shock velocity

$$u_s^2 = V_o^2 \left(\frac{P_1 - P_o}{V_1 - V_o}\right) \tag{3.6}$$

and particle velocity

$$u_p^2 = (V_o - V_1)\,(P_1 - P_o) \tag{3.7}$$

These expressions are particularly useful for clarifying the relationship between shockwaves and thermodynamic properties. Consider the dashed line AB in Fig. 3.4 connecting the initial Hugoniot point P_o V_o to P_1, V_1. The slope $(P_1 - P_o)/(V_1 - V_o)$, referred to as the Rayleigh line, is related to the square of the shock velocity according to Eq. 3.6.

If the material is initially at rest the kinetic energy acquired by compression of the piston

$$\frac{u_p^2}{2} = \frac{1}{2}\,(P_1 - P_o)\,(V_o - V_1) \tag{3.8}$$

is equal to the crosshatched area. If $P_1 >> P_o$ then from Eq. 3.4 the area is approximately equal to the increase in energy,

$$E_1 - E_o = \frac{1}{2}\,P_1(V_o - V_1)$$

and

$$E_1 - E_o = \frac{U_p^2}{2} \quad . \tag{3.9}$$

It can be shown that in the weak limit ($P_1 \rightarrow P_o$) shock compression is isentropic. Hence Eq. 3.6 reduces to

$$u_s = V_o \sqrt{\frac{P_1 - P_o}{V_1 - V_o}} \rightarrow V_o \sqrt{-\left(\frac{\partial P}{\partial V}\right)_s} = C \quad ,$$

and the initial shock velocity approaches the sound speed (C).

The entropy of the compressed fluid increases as the shock pressure increases. This results in a large increase in temperature and demonstrates the irreversible nature of the shock process. Figure 3.5 compares the calculated temperatures and pressures for isentropically and shock compressed liquid hydrogen.

3.2 Structure of a Shock Front in a Liquid

In the derivation of the Hugoniot equations the shock front has been treated as a discontinuous surface. In fact this region must be likened to a transition zone in which molecules are rushing in with a

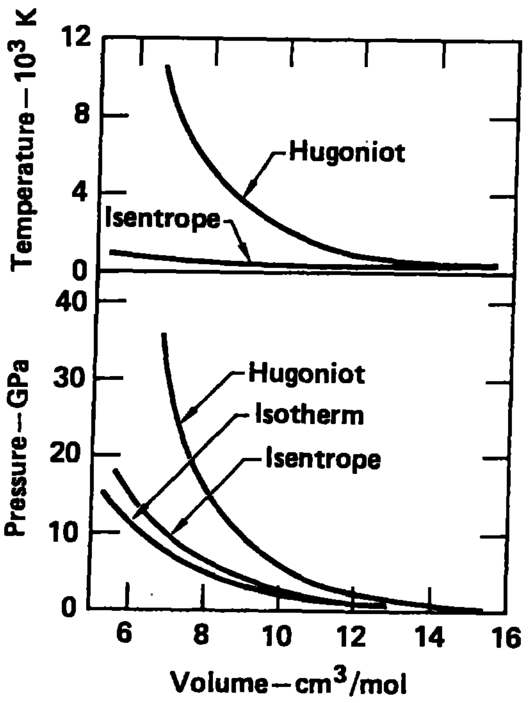

Fig. 3.5. The Hugoniot, isotherm and isentrope of molecular hydrogen illustrate the large pressure and temperature rise that accompanies shock compression. Liquid hydrogen $V_0 = 28.4\ cm^3$/mole.

Boltzmann distribution at the initial temperature and rushing out at a Boltzmann distribution at the shock temperature. The passage is irreversible and accompanied by a large entropy change. Through this transition zone there occur dissipative processes associated with viscosity and thermal conductivity. Experimental methods are not capable of directly probing the structure of shock front. Thus to properly describe the microscopic nature of shock compression it is necessary to study the process using molecular dynamics.

Klimenko and Dremin[18] started with a 2592 molecule of equilibrium liquid argon initially at $V_0 = 36cm^3$/mole, $T_0 = 131$ K, and $P_0 = 145$ atm. The atoms interact through a Lennard Jones potential. To produce a shockwave a layer of particles at one end of the cell is set in motion with a velocity u_p in the x-direction. This piston compresses material before it and propagates a shock wave down the cell. After a time interval the process reaches a steady motion and the density temperature and pressure profiles shown by the solid curves in Fig. 3.6 were calculated.

The material is compressed rapidly to a width of about 10 Å (3 atomic diameters) within a time of about 10^{-13} sec. This time is comparable to the translational relaxation time and prevents complete equilibrium in the front. This results in significant overheating of the temperature T_x in the direction of propagation (not shown). T_z (shown) is the temperature parallel to the front.

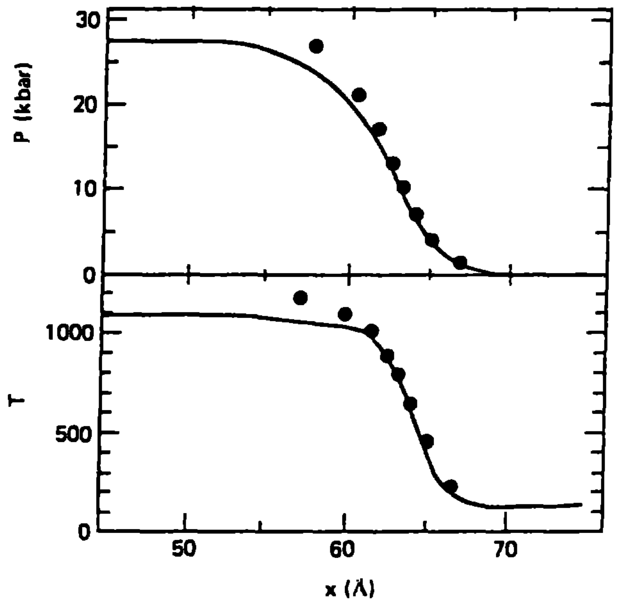

Fig. 3.6. Pressure and temperature profiles argon taken from Refs. 18 and 19. The full curves are the results from atomistic molecular dynamics. The dots are the solution of the Navier-Stokes equations. Pressure in kilobars, and temperatures in Kelvins are given as functions of distance (angstroms). The full curves include, from the Navier-Stokes viewpoint, the bulk-viscosity contribution to the mean pressure. The data correspond to a shock velocity of 2.6 km/sec.

In contrast to molecular dynamics, continuum mechanics ignores atomic structure and describes material properties in terms of continuous gradients of mass momentum and energy. Properties such as viscosity and thermal conductivity are assumed rather than derived and are determined from gradients of the velocity and temperature. Macroscopic theory should apply best to conditions where gradients are small. Hoover[19] and coworkers[20] have shown that despite these apparent limitations calculations of the shock profile using the continuum Navier-Stokes equations agree well with those of molecular dynamics simulations.

Just why the agreement is as good as it is over such a wide range of fluid conditions has not been explained.[20] Theoretical efforts to go beyond the Navier-Stokes level have not been completed yet.

4. SHOCK COMPRESSION OF SIMPLE LIQUIDS

Theoretical and experimental studies have been carried out on a wide range of shock compressed liquids. Space limitations require us to restrict the discussion to a few materials which best illustrate some particularly unique or interesting physics. Because of their simplicity it is appropriate to begin with a discussion of the rare gas liquids. We follow these with discussions of successively more complicated molecules.

4.1 Argon and Xenon

The static diamond cell and shockwave techniques for studying the properties of matter at very high pressure have so little in common that it may not be apparent to the nonspecialist that the two methods can be used to generate equation of state data that are directly comparable. Recently diamond-window cell measurements for argon have been pursued to 800 kbar at 298 K. These measurements provide an excellent opportunity to study their intermolecular forces and to compare shock and static methods for a simple system.[21]

A Comparison of Static and Shock Measurements

In the diamond-window static high-pressure cell the faces of two opposing diamond anvils are squeezed together and isothermally compress a sample of a few microns in size to megabar pressures. The sample density is determined from a direct x-ray measurement of the unit cell volume. Pressure may be determined routinely to high accuracy by measuring the density of a secondary standard such as NaCl or by recording the shift of the R_1 ruby fluorescence line. The pressure dependence of the ruby line has been calibrated against isotherms reduced from shock data.

In contrast to static methods shockwave experiments create high pressures by introducing a rapid impulse into a sample by the impact of a high speed projectile. The pressure, energy and compression are determined directly from the measurement of the shock and particle velocity and a knowledge of the initial conditions. Determination of the shock pressure is absolute and does not require a secondary standard. This feature has made shock data valuable for independent static pressure calibrations. In the case of liquid argon the final temperatures are on the order of several tens of thousands of degrees. The very different nature of the final states makes any direct comparison heavily reliant on theoretical methods. In this regard argon has several useful features. It is a relatively simple inert gas atom with a large electron band gap. The forces between atoms can be approximated by an effective pair-wise additive interactions so that established methods in statistical mechanics provide a convenient means for calculating thermodynamic properties.

Shock compression experiments on liquid argon have been carried out by several workers.[14,22] Nellis and Mitchell[14] using the two stage light-gas gun at Livermore, achieved final pressures up to 900 kbar and temperatures calculated to be approximately 30000 K. Recently Grigoriev et al.,[23] have reported measurements of a liquid argon Hugoniot to 670 kbar and the first shock temperature measurements on this substance. In the range above 400 kbar the temperature is over 13000 K and is sufficiently high to cause an appreciable degree of electronic excitation. Below this pressure, argon behaves as an insulator and the only contribution to the thermodynamic properties

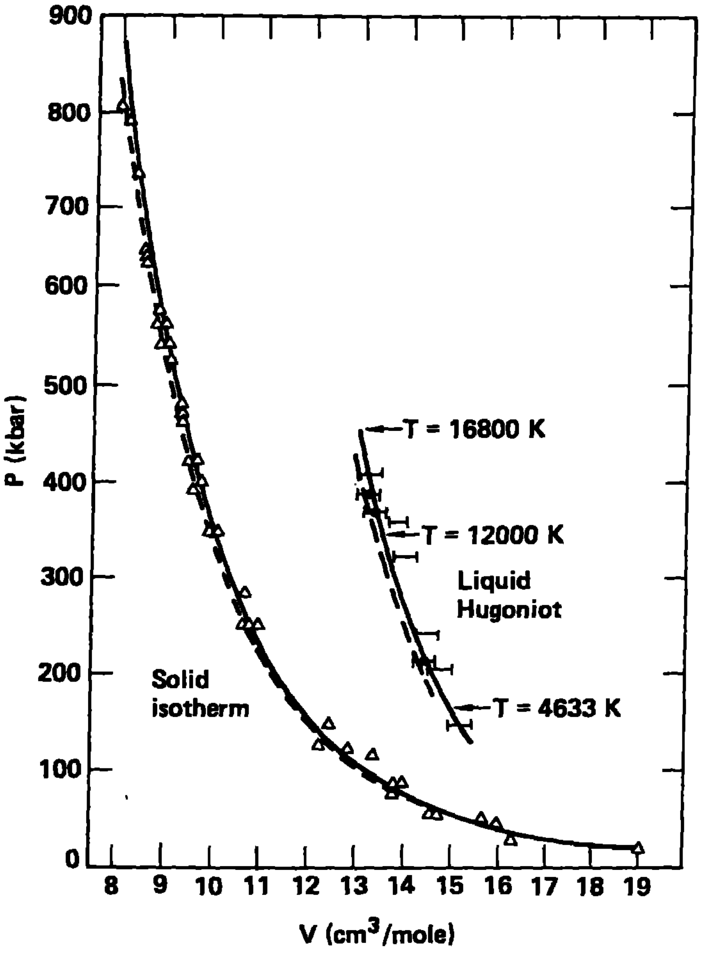

Fig. 4.1. A comparison of static (triangles), shock-wave (bars) and theoretical (curves) results. Dotted bars (|-●-|) are shock data from Ref. 14 and bars (|--|) are from Ref. 23. Solid curves were calculated using the exp-6 with $\alpha = 13.2$ and dashed curves with $\alpha = 13.0$. The initial conditions of the shock-compressed liquid are at 87 K and 28.64 cm^3/mol.

are from atom-atom interactions and atomic motion. It is these data, below 400 kbar and uncomplicated by thermal electron excitation, that provide a determination of the interatomic potential and a direct comparison with the room temperature isotherm.

Monte Carlo calculations of the pressure and energy were made using the exponential-six potential (Eq. 2.16) with parameters $\varepsilon/k=122K$, $r^* = 3.85$ Å and using two different values of α(13.2 and 13.0).

Starting from a set of initial conditions, a Hugoniot curve is determined using an equation-of-state model (in this case the Monte Carlo method) by first choosing a final state volume and then iterating on the temperature until the calculated values of E and P satisfy Eq. (3.4). The Hugoniots and isotherms calculated using these

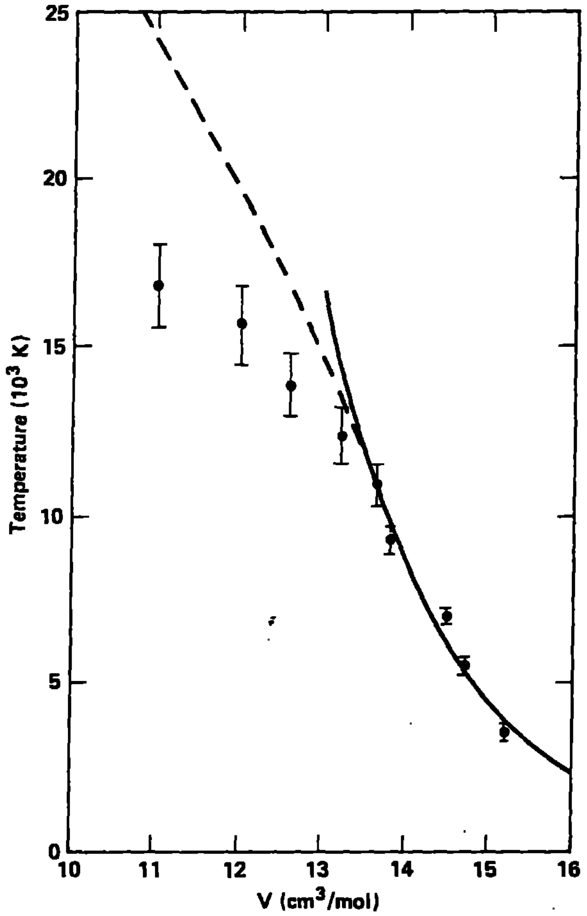

Fig. 4.2. A comparison of the measured and theoretical shock temperatures. The solid curve represents Monte Carlo results (α = 13.2) which do not include electronic excitations. The dashed curve includes electronic excitations. The bars are experimental data from Ref. 23.

potentials are shown in Fig. 4.1. T_0 and V_0 for liquid argon are 87 K and 28.64 cm^3/mol respectively. The best fit to the shock data of Nellis and Mitchell and to the diamond-window cell measurements is given by the exp-6 with an α = 13.2. The curves calculated using α = 13.0 are within the experimental precision but lie on the lower pressure side. The newly reported Soviet measurements[23] are in substantial agreement with the present results although their data is shifted on average to slightly higher pressures. The curves calculated using the two values of α provide a measure of the agreement between two very different sets of experimental data and of the uncertainty to which an effective potential can be determined.

An important feature of the shock process that provides a particularly sensitive probe of the interatomic forces at small separations is the high temperature that is generated along with the

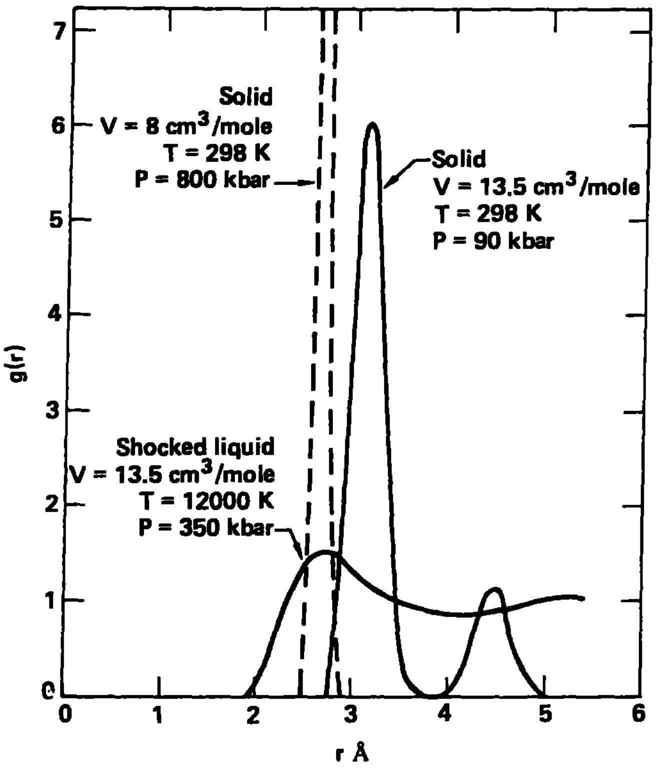

Fig. 4.3. A comparison of the calculated argon pair distribution function, g(r) for the statically compressed solid and shock compressed liquid.

high pressure. Grigoriev et al., determined the shock temperatures by measuring the emitted radiation and comparing these values to a standard pyrometer. The measured and calculated shock temperatures are shown in Fig. 4.2. Shown are the Monte Carlo results for α = 13.2 which do not include electronic excitation (solid curve) and the temperatures from an argon Hugoniot calculation which does include these excitations (dashed curve). Above 13000 K (400 kbar) the electronic excitation begins to absorb a significant amount of the shock energy which leads to a lowering of the temperature. The measured values fall significantly below those predicted by theory. The Soviet authors found the same result and have explained this as due to electron screening of the emitted shock radiation. Below 400 kbar where these effects are small the agreement between theory and temperature measurements is excellent. In the next section we return to consider the higher temperature partially ionized argon. The overall agreement between shock and static data is excellent despite the appearance of some excessive scatter in the diamond window results between 100 and 200 kbar. The goodness of the agreement lends credence to the validity of the ruby scale at these pressures to an accuracy within 10%.

The importance of temperature in the study of intermolecular

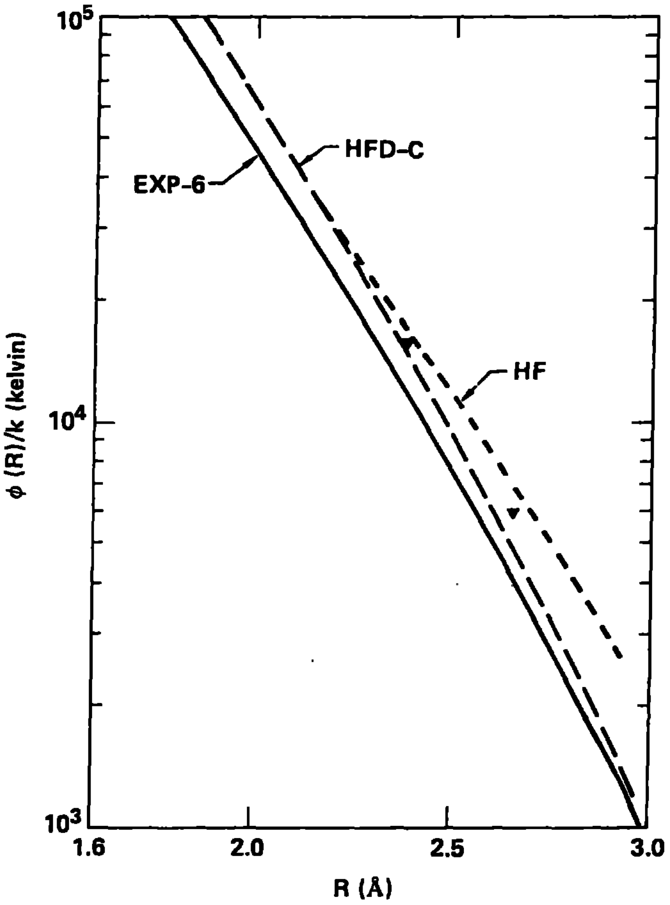

Fig. 4.4. Pair potentials $\phi(R)/k$ in units of degrees kelvin plotted versus interatomic separation. Curves are discussed and referenced in the text. HFD-C is a purely two-body potential and exp-6 is the best fit to both static and shock data. The difference between the two curves represents the softening due to many-body interactions. Also shown are Hartree-Fock (HF) results. The triangles represent configuration interaction (CI) results.

forces is well illustrated in Fig. 4.3 which shows the pair distribution in the fluid at 350 kbar and 12000 K, and in the 298 K solid at the same volume (13.5 cc/mole) and at the highest density reached in the diamond cell (8.0 cc/mole). These curves identify the range of separations probed in the various experiments. As expected, the angle-averaged pair distribution of atoms in the solid are sharply peaked at separations corresponding to nearest neighbor shells whereas the fluid distribution is smeared over a wide range of separations. The first maximum in the shocked fluid appears near 2.6 Å which is about the same position as in the solid at 8 cc/mole and 800 kbar. But, the atoms in the fluid have a much higher kinetic energy and as a result undergo collisions at much shorter separations which probe the potential down to 2 Å. It is this feature that provides the information needed for extrapolating the isotherm to much higher compressions.

The exp-6 potential has been characterized as an effective pair-potential because it includes in a phenomenological fashion the effects of the many-body interactions while retaining the convenient features of a two-body function. For this reason it is of interest to compare the present results to those for a purely two-body potential. Figure 4.4 compares our best fit, exp-6(α = 13.2), with the two-body potential of Aziz and Chen[24] (HFD-C, their designation) which they obtained by fitting to second virial coefficients, gas phase transport data and to Hartree-Fock atom-atom calculations at small interatomic separations. Also shown are the Hartree-Fock results of Gilbert and Wahl[25] and Christianson et al.[26] Two CI calculations of Wadt[27] lie between the Hartree-Fock and HFD-C curves. The difference observed between the exp-6 and HFD-C must be attributed to an effective softening of the short range repulsion by many body interactions. These results are similar to those shown for hydrogen in Fig. 2.3 in which the short range potential derived from shock data has also been found to lie well below the two-body potential.

Electronic Energy Levels and Metallization

At pressures up to 400 kbar electronic thermal excitations in shock compressed argon are negligible and this substance remains a simple closed shell insulator fluid whose properties are determined by the repulsive pair potential. Above this pressure the temperature is greater than 12000 K and rising exponentially with compression. In this higher temperature regime the properties are increasingly dominated by electron thermal excitations from the closed 3p shell into the 3d conduction band. A proper calculation of the Hugoniot requires a knowledge of the density dependence of these energy levels.

The Wigner Seitz (WS) method has been used to calculate the

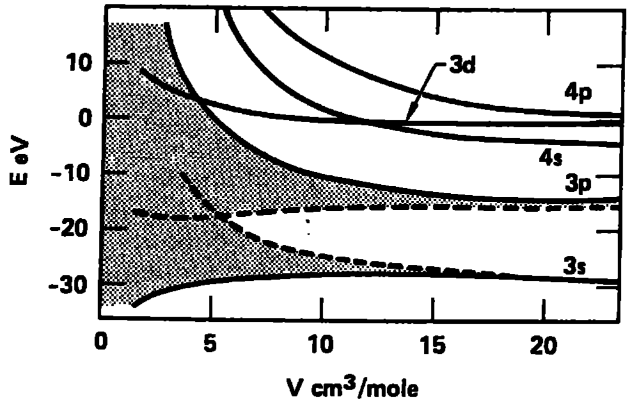

Fig. 4.5. Calculated Wigner-Seitz energy levels of argon with atomic notations. Solid curves are solutions for k = 0. Dashed curves show bandwidth based on the estimate of the energy at the maximum k value.

electronic energy levels for compressed argon as a function of volume.[28] Although less rigorous than more modern methods the results shown in Fig. 4.5 provide a simple illustration of the changes in electronic structure with compression. At normal solid density the lowest the 3d state is filled and the lowest excited state is the 4s-like conduction band. The effect of compression is to raise the energy of the 3p and 4s relative to the 3d which at high compression becomes the lowest excited state. The d state wavefunction is relatively localized and unperturbed by compression. The calculations predict that the 3d and 4s levels will cross at a volume of 4.5 cm^3/mole. At this volume argon should become metallic. McMahan[21] has carried out extensive electron band theory calculations which predict argon will undergo a structural transition from fcc to hcp at a pressure below 2.3 Mbar with a volume change less than 0.1%. The energy differences between these phases are too small to permit a more precise prediction. McMahan also predicts that hcp argon will become metallic at 4.3 Mbar and fcc argon at 5.5 Mbar as the result of a band gap closure. The transition from fcc to hcp, if it occurs, is not expected to increase the pressure by more than 0.4% and should be easily identified.

Hugoniot calculations were made for a model that treats the electron thermal properties using semiconductor statistics, and computes the fluid properties with a fluid variational theory employing the exp-6 interatomic pair potential. The intermolecular forces are assumed to be unaffected by the electronic excitation. The total energy and pressure of the fluid are written

$$E(V, T) = E_{ins}(V, T) + \Delta E(V)\, N_e(V, T) + E_e(V, T), \tag{4.1}$$

$$P(V, T) = P_{ins}(V,T) - \frac{\partial \Delta E}{\partial V} N_e(V, T) + P_e(V,T), \tag{4.2}$$

where number of electrons N_e thermally excited to the conduction band is determined using semiconductor theory.

$$N_e(T, V) = 2(g_v g_c)^{1/2} \left(\frac{2\pi kT}{h^2}\right)^{3/2} (m_v^* \, m_c^*)^{3/4}$$

$$\times \exp\left[-\left(\frac{\Delta E(V)}{2kT}\right)\right] \frac{V}{N} \quad . \tag{4.3}$$

$\Delta E(V)$ is the volume-dependent gap. The E_e and P_e are the thermal energy and pressure, respectively, of the free electrons and holes. The effective masses, m_v^*, are taken to be m_e, the free-electron mass. The band degeneracies are g_v and g_c. E_{ins} and P_{ins} are the atomic properties treated as an insulating fluid and computed using the fluid-variational theory.

Theoretical calculations are compared with experimental data[30] in Fig. 4.6. The upper curve INS (for insulator) was computed using the exp-6 pair potential and does not include electronic excitations. The

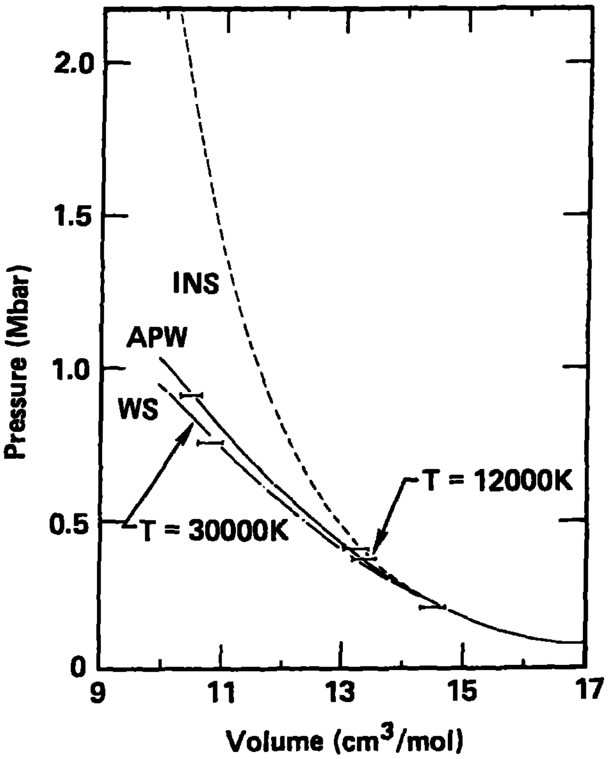

Fig. 4.6. Experimental and theoretical argon Hugoniot data plotted as pressure versus volume. V_0 = 28.6 cm^3/mole. Experimental results are shown with error bars. Theoretical curve labeled INS was computed using an intermolecular potential and does not include electronic excitations. The curves labeled WS and APW refer to Hugoniots calculated using conduction band gaps predicted by the Wigner-Seitz and augmented plane wave (APW) methods.

two lower curves include electronic thermal excitation calculated using an electron band gap. The maximum electronic excitation encountered in argon near 1 Mbar less than 0.12 electrons/atom, out of a possible 6 in the full p shell, at the highest temperature.

By absorbing some of the shock energy, the excited electrons act as thermal sinks, keeping the temperature down and lowering the pressure. The volume dependence of the energy gap also plays an important role. Because the 3p-3d gap is narrowing with decreasing volume, it makes a negative contribution to the total pressure in Eq. 4.2, lowering it further. These electronic thermal processes lead to the observed softening of the experimental Hugoniot and shock temperatures. Similar results have been observed in xenon which are due to thermal excitation of electrons from the 5p to 5d states.[31]

Xenon, which has a filled 5p band and empty 6s and 5d-conduction levels is of particular interest because it has the smallest conduction band gap and is the leading candidate for metallization among the rare gases. Band calculations predict that for an fcc lattice under compression, the energy levels of the d-like conduction band will overlap those of the 5p core and xenon will become metallic at a pressure above 1.3 Mbar.[31]

CsI which is isoelectronic with Xe is expected to demonstrate similar electronic properties. Predictions have been made that CsI will become metallic near 1 Mbar as a result of the closure of the 5p to 5d gap. Williams and Jeanloz[32] measured the optical absorption edges of CsI to 0.9 Mbar using a diamond anvil cell and Reichlin et al.[33] measured the optical reflectivity to 1.7 Mbar. These results lead to a best estimate of 1.1 ± 0.1 Mbar for the insulator to metal transition.

4.3 Molecular Hydrogen

The equation of state (EOS) of hydrogen at very high density is of considerable theoretical interest and is important for modeling of giant planet interiors. Theoretical studies indicate that at sufficiently high pressures, between 2 and 4 Mbar molecular hydrogen will undergo a phase transition into a metallic state.

Static measurements for molecular hydrogen have been made on the solid up to 370 kbar by van Straaten et al.[34] and to 200 kbar by Shimizu et al.[35] These recent studies, both using the diamond anvil cell, represent an order of magnitude extension of the pressure range over earlier work.

Shockwave data has been reported for deuterium to 750 kbar and seven times liquid density and for hydrogen to 110 kbar and three times liquid density.[36] In these experiments temperatures up to 7000 K are achieved, thereby probing the potential to intermolecular separations of about 1.5 Å. This is approximately the nearest neighbor separation of molecules in the vicinity of the metallic transition. However, the shock data provides little information about the potential nearer the attractive well at low energies, and this information is best obtained from static experiments.

Intermolecular potentials

The experimental H_2 and D_2 Hugoniot data has been analyzed using several different H_2-H_2 potentials. The first of these is the potential of Silvera and Goldman (SG)[37] who used it to explain the available static compression data. The SG potential $\phi_{SG}(r)$ consists of two terms, i.e.,

$$\phi_{SG}(r) = \phi_p(r) + \phi_t(r) \quad . \tag{4.4}$$

Silvera and Goldman associate $\phi_p(r)$ with the potential of an isolated H_2-H_2 pair and $\phi_t(r)$ with the "average" contribution by the Axelrod-Teller triple dipole intraction. They are given, respectively, by

$$\phi_p(r) = \exp(\alpha - \beta r - \gamma r^2) - \left(\frac{C_6}{r^6} + \frac{C_8}{r^8} + \frac{C_{10}}{r^{10}} \right) f(r) \ , \tag{4.5}$$

$$\phi_t(r) = \frac{C_9}{r^9} f(r) \quad . \qquad (4.6)$$

where the modulation function f(r),

$$f(r) = \exp\left[-\left(\frac{1.28\ r_m}{r} - 1\right)^2\right] \ , \ r \leq 1.28\ r_m \ ,$$
$$= 1 \ , \qquad r > 1.28_m\ r \ , \qquad (4.7)$$

attenuates the long-range multipole terms at small r. The factor r_m is the position of the attractive minimum of $\phi_p(r)$. The SG potential has been found to reproduce both the melting properties and the static compression data of liquid H_2 and D_2 at 75-300 K to 2 GPa. However, it becomes less suitable to explain the high pressure static and the dynamic data. To remedy this, $\phi_{SG}(r)$ was modified by softening it at small r.[38]

Fluid theory and Hugoniot calculations[38]

The thermodynamic properties were calculated using the Helmholtz free energy (A) given by

$$A = 2.5\ NkT + N[0.5\ h\nu + kT\ \ln\ [1 - \exp(-\ \beta h\nu)]]$$
$$+ A_{int} + NkT\ \ln\ \rho + \text{constant}, \qquad (4.8)$$

The first term is due to the kinetic energies of translation and rotation; the second term, within the bracket, represents the free energy of a vibrating molecule with frequency $h\nu/k$ = 6340 K and 4395 K for H_2 and D_2, respectively. The term A_{int} is the intermolecular potential energy contribution evaluated from fluid variational theory:

$$A_{int} = A_{HS}(\eta) + F(\eta)\ NkT$$
$$+ (\rho N/2) \int dr\ \phi\ (r)\ g_{HS}(r,\ \eta) + A_{QM} \quad , \qquad (4.9)$$

The last term A_{QM} is the first-order quantum mechanical correction to A in the Wigner-Kirkwood expansion. It makes a negligible contribution under the experimental shock-wave conditions except at the initial states of liquid H_2 and D_2.

Figure 4.7 compares the experimental liquid D_2 Hugoniot with theoretical calculations using the modified SG potential which agree satisfactorily with the data over the entire range. The Hugoniot calculated with the unmodified SG potential are too stiff. Molecular dissociation was found to be negligible except on the double shocked Hugoniot at 75 GPa where it leads to a 1% decrease in the volume which is well within experimental error.

Calculated solid isotherms for hydrogen are shown in Table 4.1 and are in agreement with the diamond-anvil experimental data of van Straaten.

TABLE 4.1. 5 K isotherms of H_2.

V (cm^3/mol)	Pressure (kbar)	
	Calculations	Experiment
10	22.6	22.7
9	35.1	34.6
8	56.2	54.1
7	89.0	87.8
6	153.	149.
5	274.	271.
4	529.	537.[a]
3	1173.	1120.[a]
2	3429.	3482.[a]
1.6	6082.	5892.[a]

[a] Extrapolated values.

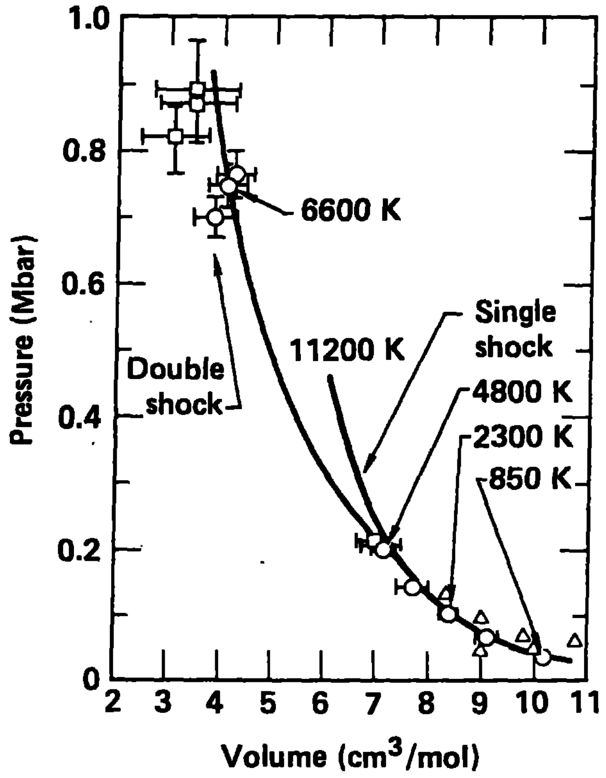

Fig. 4.7. Single and double-shocked deuterium Hugoniots.

Metallic Transition

The possibility exists that hydrogen may become a metal by dissociation into a monatomic phase or, as in the case of iodine, first convert to an electrically conducting molecular phase as a result of energetically overlapping valence and conduction bands. The conducting molecular phase would then convert into a monatomic metal at some higher pressure. Electron band calculations predicted a band crossing in the molecule at 2.4 cm^3/mol,[39] or 210 GPa (2.1 Mbar) on our theoretical curve.

The molecular-to-metallic first-order phase transition was estimated using ϕ to obtain the properties of solid H_2. The transition pressure, predicted by equating the pressures and the Gibbs free energies, is estimated to be between 3.1 and 3.6 Mbar. These values suggest that an insulating molecular-to-metallic molecular transition will first occur followed at higher pressure by the diatomic to monatomic metal transitions.[38]

4.4 The Dissociation of Dense Liquid Nitrogen

The dissociation of molecular nitrogen has been the subject of several recent experimental and theoretical studies. McMahan and LeSar[40] predicted that the molecular solid at 0 K should dissociate to a monatomic phase near 0.8 Mbar. However subsequent diamond-anvil cell studies have shown no evidence for such a transition up to 1.3 Mbar. The failure to observe this transition has been attributed to a large energy barrier between the two phases. In a series of papers Nellis et al.[41] have reported shockwave results which indicate that liquid nitrogen begins to undergo a transformation at a pressure of 0.31 Mbar and a temperature of about 7000 K. The most likely explanation is that they have observed molecular dissociation.

In the simplest model, the one which neglects dissociation, the intermolecular potential is described by a spherical angle averaged interaction which neglects the diatomic structure of the molecule. The parameters were chosen to scale from the argon potential by the use of the law of corresponding states. The vibrational and electronic energy levels are taken to be the free molecule values.

The calculated principal Hugoniot shown in Fig. 4.10 (curve A) is in good agreement with the data of Nellis et al.[41] up to about 310 kbar. Above this pressure the theoretical curve continues to rise rapidly but fails to exhibit the large increase in compressibilty observed experimentally. Clearly this model is incomplete because it fails to incorporate dissociation.

Consider a reacting mixture of atoms and molecules. Let x be the fraction of molecules that have undergone dissociation into atoms. We write F the free energy per two atoms as;

$$F = (1 - x)\,F^0_{N_2} + xF^0_{2N} + F_{mix} + A_{int}, \tag{4.10}$$

where $F^0_{N_2}$ and F^0_{2N} are respectively the free energies of the isolated

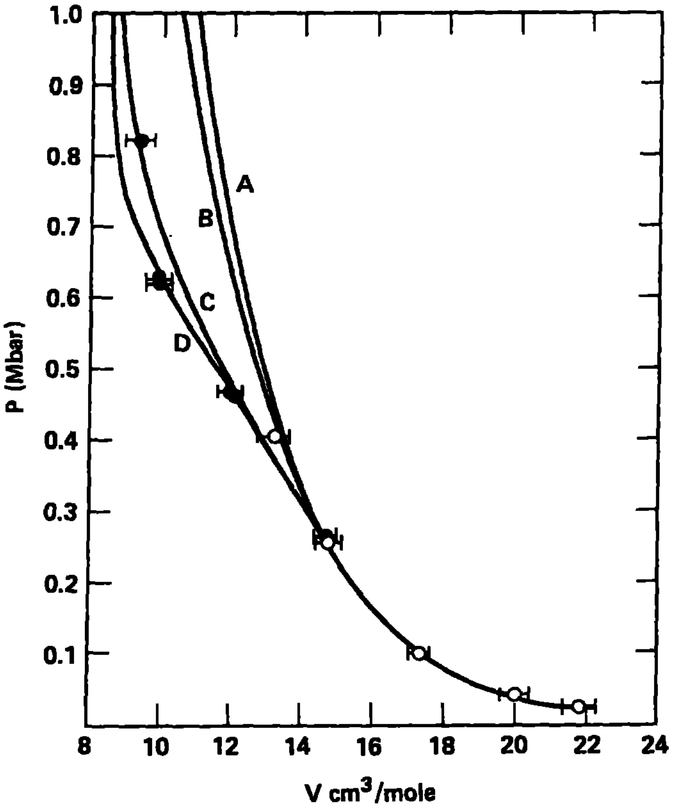

Fig. 4.8. Nitrogen Hugoniots, $V_0 = 34.7$ cm^3/mole. Theoretical curves: (A) with no dissociation; (B) including dissociation with dissociation energy 9.76 eV; curves C and D include dissociation with atomic phase binding energy.

molecule and of two atoms. F_{mix} is the free energy of mixing. Minimization of F determines X. A_{int} is the potential energy of the fluid calculated using fluid variational theory. The results (curve B) differ only slightly from curve A which neglects dissociation.

There are a number of reasons why the present model might fail even when the dissociation energy is included. One is that some of the energy levels of the pure components may be density dependent. But the most likely cause probably stems from the neglect of the atomic phase binding energy. In the gas phase 9.76 ev are required to break the chemical bond and move the atoms to infinite separation. Clearly this value cannot be correct in the very dense fluid because it does not account for the recombination of atoms into other chemical states. This binding would return some of the energy expended in the bond breaking and decrease the energy needed for dissociation. An analogous effect known as 'ionization lowering' is observed in dense plasmas where the interaction of the ionized electron with the remaining particles leads to a lowering of the effective ionization energy. We may refer to the molecular analog as 'dissociation lowering.' As an example consider the case in which the molecule is compressed to such a high density that the molecular bond distance becomes comparable to the intermolecular separation. At this density much less than 9.76 ev would be required to dissociate the molecule. Thus we may conclude that the dissociation energy should decrease continuously from the gas phase value to some much smaller figure at high density.

We introduce this reasoning into our thermodynamic model by adding to the free energy a volume dependent term E_b equal the binding energy of the atomic phase per two atoms. It contributes to the total free energy in proportion to the fraction of molecules dissociated.

$$F = (1-x)F^0_{N_2} + xF^0_{2N} + F_{mix} + A_{int} + xE_b \quad . \tag{4.11}$$

The volume dependence leads to an additional term in the pressure equation:

$$P = RT/V(1+x) + P_{int} - \left(\frac{\partial E_b}{\partial V}\right)x \tag{4.12}$$

and to a volume dependent dissociation energy

$$D = 9.76 + E_b. \tag{4.13}$$

Since E_b has a negative value it lowers the dissociation energy and leads to an increase in the dissociation fraction. E_b is determined by fitting to the Hugoniot and is consistent with the calculated cohesive energy for atomic nitrogen.

The introduction of a binding energy for the atomic phase results in the softening of the Hugoniot shown as curve C (or D). The calculated values of the dissociation energy and the fraction of molecules dissociated are plotted in Fig. 4.9. Fig. 4.10 is an overview of the nitrogen equation of state for the present model showing the 0 K molecular and metallic isotherms and the Hugoniot. Also shown are the results of McMahan who has calculated isotherms for atomic nitrogen in several different crystal structures. The overall agreement of the theoretical model with McMahan's results are consistent with what one would expect from having determined empirically the binding energy from expanded metal data. Physically what is happening is that every time a molecule dissociates, the two atoms are converted into metal atoms lying on a much lower isotherm. Thus the dissociation process leads to a drop in pressure or equivalently to a volume collapse. An analogous behavior is that observed in shock compressed liquid argon and xenon. In these liquids electrons are thermally excited from the top of a filled p-like valence band to the bottom of an unfilled d-like conduction band in which they have a lower pressure. The energy band gap separating these two states is decreasing with decreasing volume and this introduces a negative contribution to the pressure just as it does in the present case. And with the same effect. The negative contribution to the thermal pressure leads to the large increase in

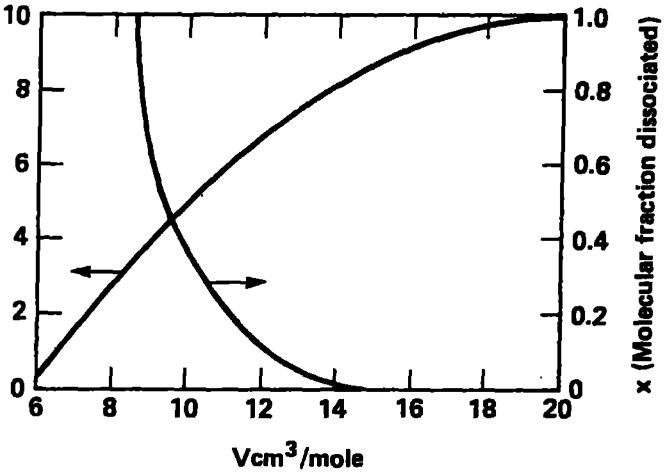

Fig. 4.9. Dissociation energies (D) and fractions of dissociated molecules (x) calculated along theoretical Hugoniot.

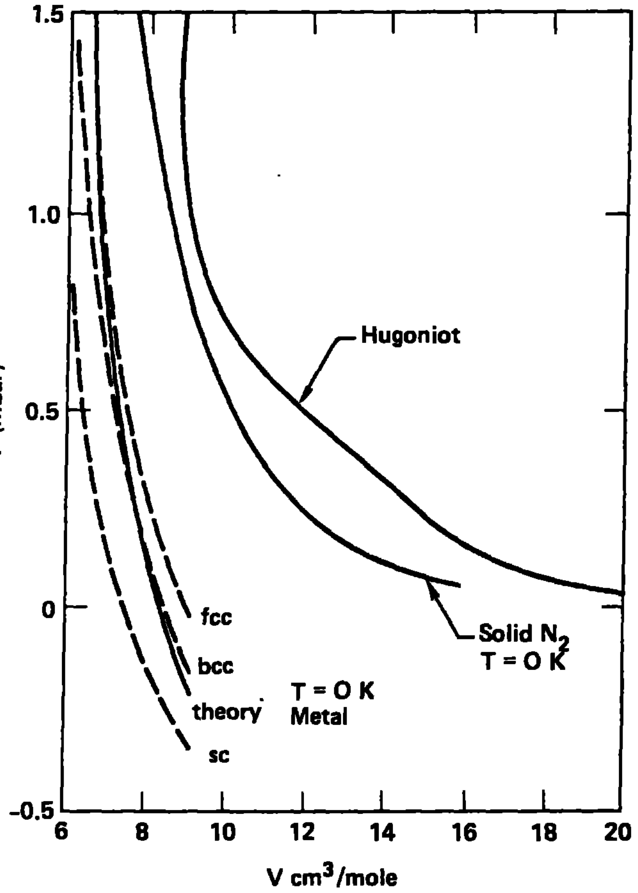

Fig. 4.10. Calculated molecular and atomic nitrogen equation of state (solid curves). The dashed curves represent the results of McMahan for the metal with different crystal structures.

the compressibility observed along the Hugoniot.

4.5 Polyatomic Molecules; Water and Ammonia.

The properties of water and ammonia have been studied with measurements

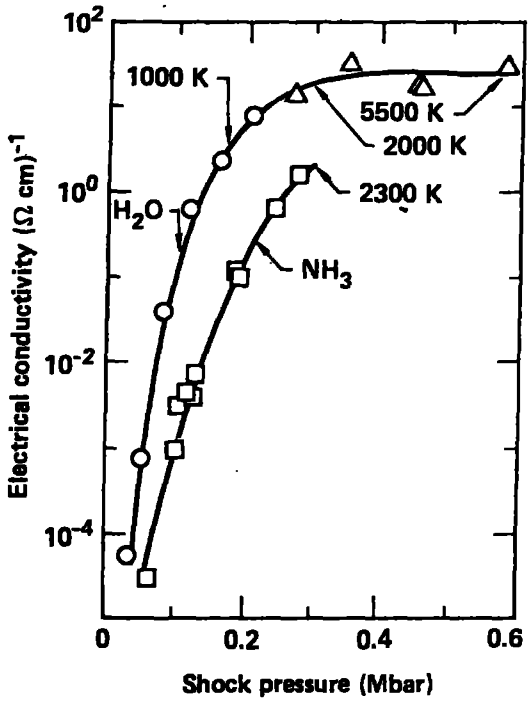

Fig. 4.11. Electrical conductivity of water and ammonia. From Ref. 43.

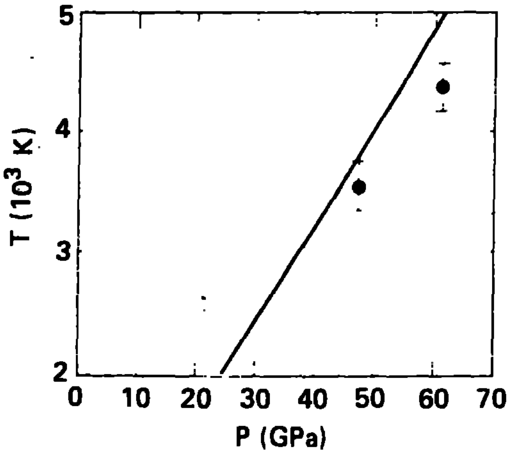

Fig. 4.12. NH_3 shock temperature plotted as a function of pressure. Solid line is a calculation using fluid variational theory. From Ref. 43.

of the Hugoniot, shock temperatures and electrical conductivities. The most interesting feature of work prior to 1979 were the early electrical conductivity measurements of Hamman and Linton[42] on water and aqueous solutions of KCl, KOH and HCL at shock pressures ranging from 70-133 kbar. By combining the measured ionic conductivities of these compounds it was estimated that the ionization of water becomes nearly complete at 200 kbar and that this transformation may be responsible for the change in the compressibility of the water Hugoniot above and below the 150-200 kbar region. The shock temperature and electrical measurements on water have been extended to 600 kbar and more recently these were made for ammonia.[43]

Comparison of the calculated temperatures with the experimental results for NH_3 in Fig. 4.12 shows that the model is in reasonably good agreement with the data. The small deviation of 10% at the highest pressure maybe an indication of an additional absorption mechanism at these high pressures. Previous electrical conductivity measurements on ammonia have shown that it becomes conductive in the range 70-280 GPa. The mechanism proposed to explain the high conductivity was molecular dissociation-ionization. The relatively small difference between the measured temperatures and those calculated using this non-dissociative model suggests that dissociation is not sufficient to affect the equation of state in a dramatic way. Including dissociation-ionization in the model would have the effect of lowering the calculated temperatures in the direction of better agreement with the experimental data.

Theoretical studies on water are complicated by strong electrostatic interactions and highly nonspherical potentials. Ree[44] has carried out a detailed study of shock compressed water using fluid perturbation theory and intermolecular potentials based on quantum mechanical ab-initio calculations. Of the several potentials examined Ree found best agreement with experiment was given by the Stillinger and Rahman ST2 potential. This is a non-spherical atom-atom potential which must be suitably averaged over all orientations of molecules 1 and 2 at fixed intermolecular separations.

4.5 Carbon Compounds

Chemical decomposition is known to occur in small molecules containing carbon and in hydrocarbons. Yakusheva et al.[45] have shown that the shock compression of many transparent and colourless hydrocarbons above about 100 kbar and 1000 K is accompanied by a break in the Hugoniot curve and a sharp increase in the light absorbance, resulting in a loss of transparency. These features suggest a rapid pyrolysis of the initial molecule and the formation of an opaque carbon condensate (i.e., tars, graphite). Liquid CS_2 exhibits similar behaviour when it is shock-compressed to approximately 60 kbar and statically compressed to about the same pressure. CO probably decomposes into carbon and CO_2.

Theoretical calculations of hydrocarbon Hugoniots, including methane, predict that shock heating induces C-H bondscission and favours the condensation of C atoms into elemental carbon.[46] The

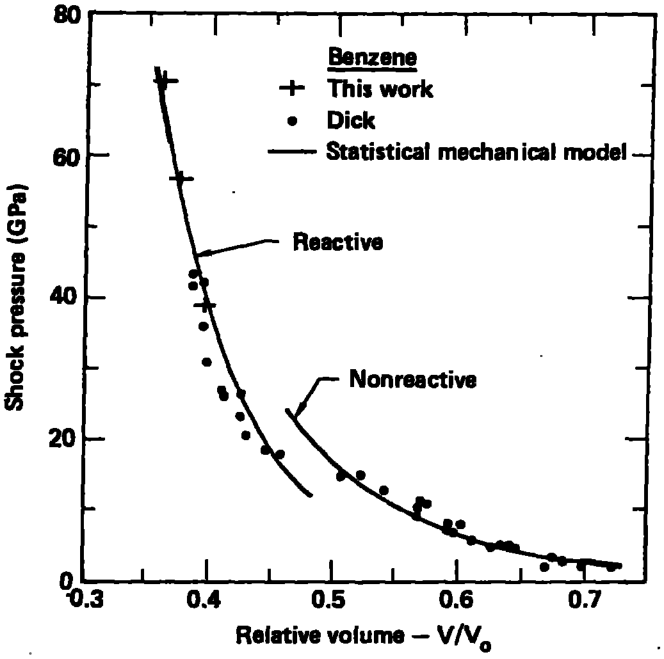

Fig. 4.13. Shock pressure vs relative volume for benzene. The curve above 20 GPa was calculated assuming decomposition. The curve below 20 GPa was calculated assuming benzene retains its C_6H_6 molecular structure. From Ref. 46.

formulation considers a chemical equilibrium involving C (diamond), C (graphite), and H_2 plus nine other low molecular-weight species, CH_4, C_2H_2, C_6H_6, C_2H_4, C_2H_6, C_3H_6, C_3H_8, C_4H_{10}, and C_5H_{12}. The concentrations are determined by minimizing the Gibbs free energy. The Hugoniot calculated for molecular benzene shown in Fig. 4.13 suggests the benzene molecule dissociates above a shock pressure of 130 kbar. Similar results have been obtained for a large number of hydrocarbons.

4.6 The Structure of Dense Alkali Halide Melts

The unique characteristic of shockwave experiments is that they can be used to explore states of matter at very high pressure and temperature that are inaccessible by other techniques. This property makes it valuable for studying melting at extreme conditions. The usefulness of shock melting data is not that it simply represents more data but that it greatly extends the range of conditions over which to test the applicability of melting laws and concepts.

When a substance melts at atmospheric pressure the added energy does not lead to a rise in temperature until the process has been completed. Under shock compression the pressure-temperature path passes through the melting curve. This feature was first observed by Kormer, et al.[47] (Fig. 4.12) in shock temperature measurements on NaCl and KCl. Similar results for CsI, have recently been obtained by

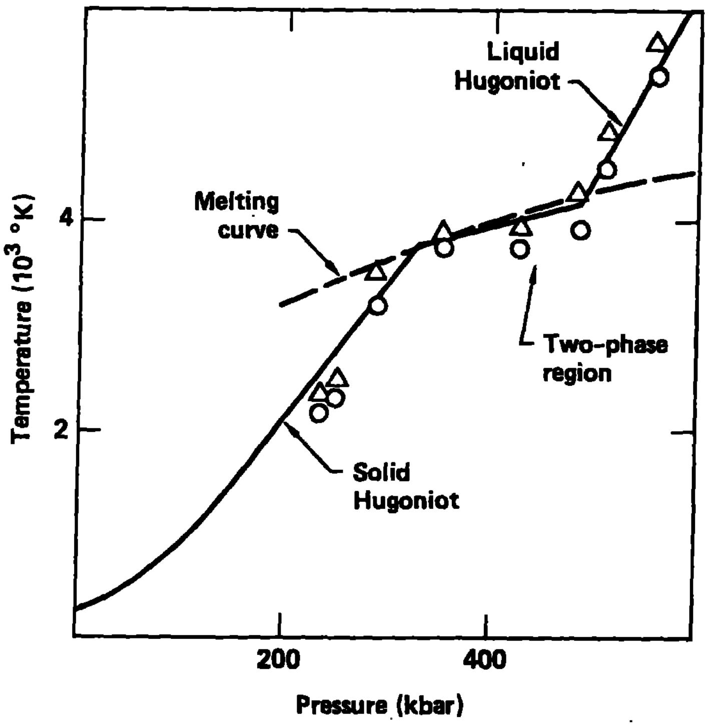

Fig. 4.14. Hugoniot temperature measurements and estimated melting curve for KCl. Copied after Kormer.

Radousky, et al.[48]

X-ray scattering and neutron diffraction experiments coupled with Monte Carlo and hypernetted chain (HNC) equation calculations have established that at atmospheric pressure alkali halide melts are characterized by a relatively open NaCl-like structure containing about 5 to 6 atoms in the nearest neighbor shell. The application of pressure is believed to result in a gradual increase in the coordination number. But very little is known experimentally.

The hypernetted chain equation is now widely used for calculating the properties of ionic fluids.[49] Calculations were made using an exponential six function to represent the pair-potential for the inert gas xenon and for CsI using an exponential-six with a coulomb term added.

$$\phi(r) = \phi_{exp6}(r) + \frac{Z_1 Z_2 e^2}{r}$$

where Z_1 and Z_2 are the ion charges. The xenon results provide a reference against which to judge the occurrence of a structural change in CsI to an inert gas-like structure.

Figure 4.15a shows the partial distribution functions of liquid CsI calculated at its normal melting temperature The atomic separations in the figure are plotted in units of r/a where a is the mean ion sphere radius, or a = $(3/4\pi V/N)^{1/3}$. For these potentials g_{++} =

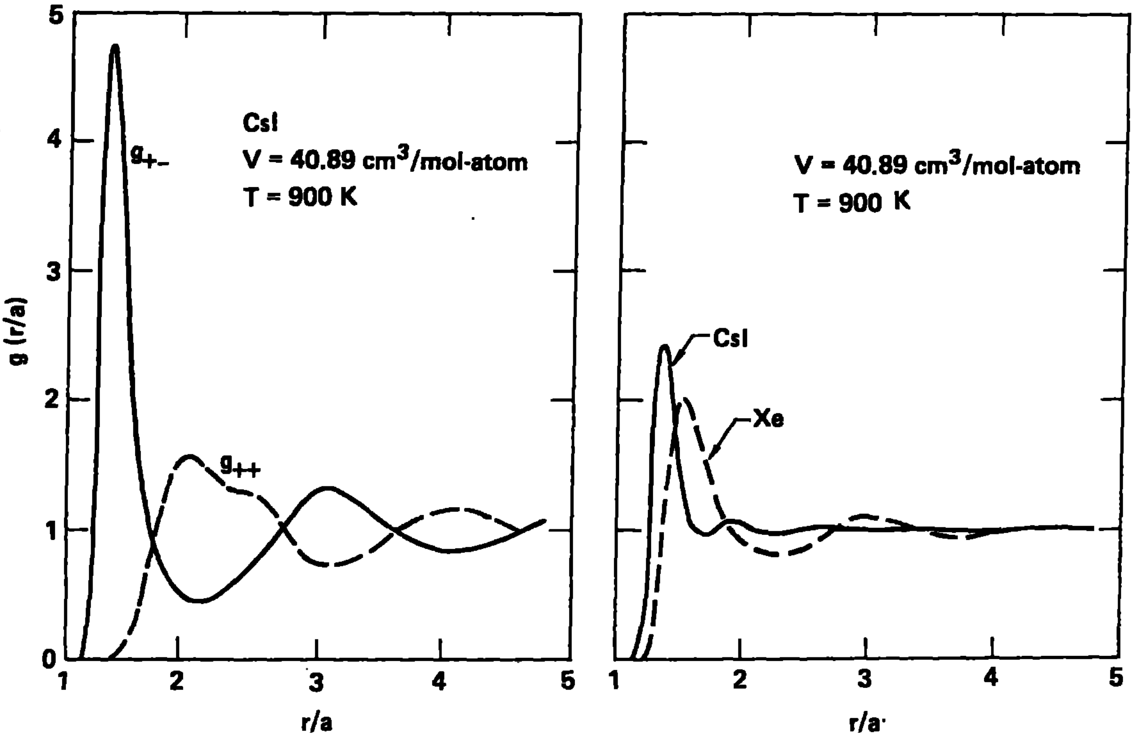

Fig. 4.15. (a) Partial distribution functions for CsI; (b) Comparison of total distribution functions for CsI and Xe. P ~ 0 kbar.

g_{--}. The figure exhibits the characteristic alkali halide arrangement of alternating shells of unlike and like charge. Figure 4.15b compares the total pair distribution function, $g(r) = (g_{++}(r) + g_{+-}(r))/2$, of CsI with that for the xenon-like fluid (potential 1). The figure shows two very different structures. The reader may have noted that there is a shoulder in the first g_{++} peak near (r/a) = 2.3. This is the start of a pressure induced splitting into two new peaks.

As the pressure along the freezing line increases the splitting of the g_{++} peak becomes more pronounced. Increasing the pressure to about 300 kbar (3650 K) to near the observed shock freezing point shifts the first g_{++} peak to inside the g_{+-} first peak envelope (Fig. 4.16a). As a result the total distribution functions of Xe and CsI (Fig. 4.16b) are now virtually identical. Each ion has about 12 nearest neighbors, as in a close-packed system, of which seven are oppositely charged and five have the same charge. Figure 4.16a demonstrates that the oppositely charged neighbors on the average approach each other more closely than do ions with the same charge. But a considerable degree of interpenetration exists. At pressures up to 700 kbar no important changes were observed.

These results demonstrate that at sufficiently high density the short range repulsive forces will be dominant over the long range attraction. Near the pressure of 300 kbar, where the Hugoniot enters

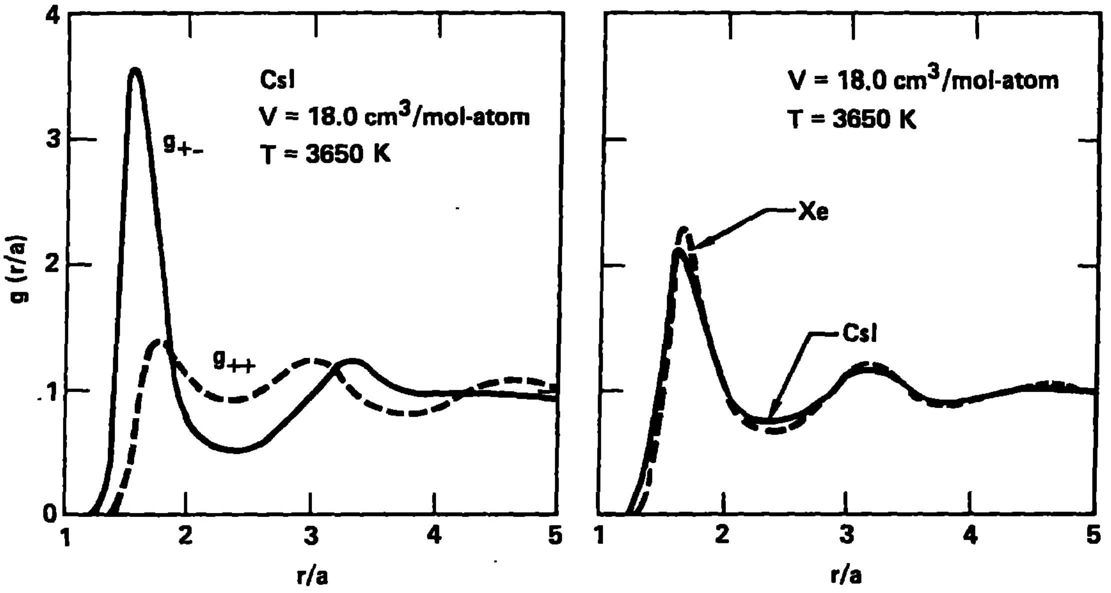

Fig. 4.16. (a) Partial distribution functions for CsI; (b) Comparison of total distribution functions for CsI and Xe. P ~ 300 kbar.

the fluid, the contribution of the exp-6 is an order of magnitude larger than that of the Coulomb term. Thus the properties are dominated by the strong repulsive forces and the liquid adopts a xenon or hard sphere-like structure. The application of pressure has the effect of "dialing down," or decoupling the influence of the coulomb forces. The results demonstrate the existence of a gradual pressure-induced shift in the structure of an alkali halide melt from an open arrangement to one characteristic of a simple non-ionic fluid. Tallon[50] has considered the possibility that the shapes of melting curves could be understood by a continuous pressure induced change in the melt to a more closely packed state. Tallon explains the curvature and projected occurrence of the maxima in terms of a continuous transition in the melt from the lower density six-coordinated state to a higher density eight-coordinated state at higher pressure. His conclusions are generally confirmed by the present results in the sense that we also believe that the fluid becomes more densely packed.

Recently several authors have suggested that liquid silicates and magmas undergo an increase in coordination number with increasing pressure.[51-52] Thus, it appears that the phenomena observed in alkali halides is not isolated but is a more general feature of ionic materials that has important consequences for geophysics.

ACKNOWLEDGEMENTS

Work performed under the auspices of the U.S. Department of Energy by the Lawrence Livermore National Laboratory under contract number W-7405-ENG-48.

REFERENCES

1. J. A. Barker and D. H. Henderson, Rev. Mod. Phys. 48, 587 (1976).
2. J. P. Hansen and I. R. McDonald, 'Theory of Simple Liquids,' Academic Press, NY, 1976.
3. M. L. Klein, Ann. Rev. Phys. Chem. 36, 525 (1985).
4. N. F. Carnahan and K. E. Starling, J. Chem. Phys. 51, 635 (1969).
5. F. H. Ree, J. Chem. Phys. 73, 5401 (1980).
6. M. Ross, J. Chem. Phys. 71, 1567 (1979).
7. W. G. Hoover, M. Ross, K. W. Johnson, D. Henderson, J. A. Barker and B. C. Brown, J. Chem. Phys. 52, 4931 (1970).
8. J. P. Hansen, Phys. Rev. A 2, 221 (1970).
9. D. A. Young and F. J. Rogers, J. Chem. Phys. 81, 2789 (1984).
10. J. Talbot, J. L. Lebowitz, E. M. Waisman, D. Levesque and J. J. Weis, to be published, J. Chem. Phys. 1986.
11. R. A. Aziz, V. P. S. Nain, J. S. Carley, W. L. Taylor and G. T. McConville, J. Chem. Phys. 70, 4330 (1979).
12. M. Ross and F. H. Ree, J. Chem. Phys. 73, 6146 (1980).
13. Ya. B. Zeldovich and Yu. P. Raizer, Physics by Shock Waves and High Temperatures Hydrodynamic Phenomena, Vols. 1-2 (New York: Academic Press), 1966.
14. W. J. Nellis, and A. C. Mitchell, J. Chem. Phys. 73, 6137, 1980.
15. M. Van Thiel, M. J. Shaner, and E. Salinas, Lawrence Livermore National Laboratory Report UCRL 50108, Vols. 1-3, Rev. 1, 1977.
16. S. P. Marsh, LASL Shock Data, (Berkeley: University of California Press, 1980).
17. L. V. Al'tshuler, A. A. Bakanova, I. P. Dudoladov, E. A. Dynin, R. F. Trunin, and B. A. Chekin, J. Appl. Mech. Tech. Phys. 22, 145, 1981.
18. V. Y. Klimenko and A. N. Dremin, in Detonatsiya, Chernogolovka, edited by O. N. Breusov et al. (Akad. Nauk, Moscow, SSSR, 1979), p. 79.
19. W. G. Hoover, Phys. Rev. Lett. 23, 1531 (1979).
20. B. L. Holian, W. G. Hoover, B. Moran and G. K. Straub, Phys. Rev. A 22, 2798 (1980).
21. M. Ross, H. K. Mao, P. M. Bell and J. A. Xu, to be published J. Chem. Phys. 1986.
22. M. van Thiel and B. J. Alder, J. Chem. Phys. 44, 1056 (1966); R. D. Dick, R. H. Warnes, and J. Skalyo, Jr., J. Chem. Phys. 53, 1648 (1970).
23. F. V. Grigoriev, S. B. Kormer, O. L. Mikhailova, M. A. Mochalov, and V. D. Urlin, Sov. Phys. JETP 61, 751 (1985), [Zh. Eksp. Teor. Fiz. 88, 1271 (1985)].

24. R. A. Aziz and H. H. Chen, J. Chem. Phys. 67, 5719 (1977).
25. T. L. Gilbert and A. C. Wahl, J. Chem. Phys. 47, 3425 (1967).
26. P. A. Christiansen, K. S. Pitzer, Y. S. Lee, J. H. Yates, W. C. Ermler and N. W. Winter, J. Chem. Phys. 75, 5410 (1981).
27. W. R. Wadt, J. Chem. Phys. 68, 402 (1978).
28. M. Ross, Phys. Rev. 171, 777 (1968).
29. A. K. McMahan, Phys. Rev. B 33, 5344, (1986).
30. M. Ross, W. J. Nellis, and A. C. Mitchell, Chem. Phys. Lett. 68, 532 (1979).
31. M. Ross and A. K. McMahan, Phys. Rev. B 21, 1658 (1980).
32. Q. Williams and R. Jeanloz, Phys Rev. Lett. 56, 163 (1986).
33. R. Reichlin, M. Ross, S. Martin, K. A. Goettel, to be published in Phys. Rev. Lett. 1986.
34. J. Van Straaten, R. J. Wijngarden, and I. F. Silvera, Phys. Rev. Lett. 48, 97 (1981).
35. H. Shimizu, E. M. Brody, H. K. Mao, and P. M. Bell, Phys. Rev. Lett. 47, 128 (1981).
36. W. J. Nellis, M. Ross, A. C. Mitchell, M. van Thiel, D. A. Young, F. M. Ree and R. J. Trainor, Phys. Rev. A 27, 608 (1983).
37. I. F. Silvera and V. V. Goldman, J. Chem. Phys. 69, 4209 (1978).
38. M. Ross, F. H. Ree, and D. A. Young, J. Chem. Phys. 79, 1487 (1983).
39. C. Friedli, and N. W. Ashcroft, Phys. Rev. B 16, 662 (1977).
40. A. K. McMahan and R. LeSar, Phys. Rev. Lett. 54, 1929 (1985).
41. W. J. Nellis and A. C. Mitchell, J. Chem. Phys. 73, 6137 (1980); W. J. Nellis, N. C. Holmes, A. C. Mitchell, and M. van Thiel, Phys. Rev. Lett. 53, 1661 (1984).
42. S. D. Hamann and M. Linton, Trans. Faraday Soc. 65, 2186 (1969).
43. H. B. Radousky, A. C. Mitchell, W. J. Nellis and M. Ross, Proceedings of the APS Topical Conference on Shockwaves in Condensed Matter, Spokane, WA (1985).
44. F. H. Ree, J. Chem. Phys. 76, 6287 (1982).
45. O. B. Yakusheva, V. V. Yakushev, A. N. Dremin, Russ. J. Phys. Chem. 51, 973 (1977).
46. W. J. Nellis, F. H. Ree, R. J. Trainor, A. C. Mitchell and M. B. Boslough, J. Chem. Phys. 80, 2789 (1984).
47. S. B. Kormer, Usp. Fiz. Nauk. 94, 641 (1968) [Sov. Phys.-Usp. 11, 229 (1968)].
48. H. B. Radousky, M. Ross, A. C. Mitchell, and W. J. Nellis, Phys. Rev. B 31, 1457 (1985).
49. M. Ross and F. J. Rogers, Phys. Rev. B 31, 463 (1985).
50. J. L. Tallon Phys. Lett. 72A, 150 (1979).
51. C. A. Angel, P. A. Cheeseman, and S. Tomaddon, Science 218, 885 (1982).
52. I. Kushiro, in Physics of Magmatic Processes, edited by R. B. Hargraves (Princeton University Press, Princeton, New Jersey, 1980), pp. 93-120.